Journal of Structural Geology 154 (2022) 104490

Contents lists available at ScienceDirect

Journal of Structural Geology

journal homepage: www.elsevier.com/locate/jsg

Geochemical and microtextural properties of veins in a potential high-level radioactive waste disposal site

Ervin Hrabovszki [a,*], Emese Tóth [a], Tivadar M. Tóth [a], István Garaguly [a,b], István Futó [c], Zoltán Máthé [d], Félix Schubert [a]

[a] Department of Mineralogy, Geochemistry and Petrology, University of Szeged, 6722, Szeged, Hungary
[b] Bay Zoltán Nonprofit Ltd. for Applied Research, BAY-BIO Division for Biotechnology, 6726, Szeged, Hungary
[c] Isotope Climatology and Environmental Research Centre, Institute for Nuclear Research, Hungarian Academy of Sciences, 4026, Debrecen, Hungary
[d] Mecsekérc Ltd., 7633, Pécs, Hungary

ARTICLE INFO

Keywords:
Vein texture
Vein growth
Microthermometry
Stable isotopes
Paleofluid transport

ABSTRACT

In this study, geochemical and petrographic characteristics of veins from the Permian Boda Claystone Formation (Mecsek Mts., Hungary) are presented. Understanding the connection between these properties is vital in the reconstruction of paleofluid history and tectonic evolution of this potential high-level radioactive waste disposal site. Each of the observed four vein generations consists of several mineral phases and has complex evolution, which can be attributed to multiple diagenetic and tectonic processes. Syntaxial and antitaxial veins have been observed suggesting oscillatory advective and diffusive material transport mechanisms; however, veins associated with mobile hydrofractures have also been detected. The parent fluids with a predominant temperature of 100–150 °C and variable salinity (3.5–13.7% $w\text{NaCl}_{eq}$) originated potentially by mixing of connate brine with freshwater released by smectite-to-illite transition and isotope exchange with sedimentary minerals, which may have caused the observed $\delta^{18}O$ values (−1.12 to 4.67‰, V-SMOW). In contrast to the most vein-filling mineral phases, a breccia cement phase precipitated from a low-temperature (<50 °C) and salinity (0.0–0.4% $w\text{NaCl}_{eq}$) meteoric fluid. In the pores of this breccia veins, late-stage fluid migration is verified. Therefore, these veins are of paramount importance for studying the isolation properties of the rock body.

1. Introduction

During the operation and future decommissioning of the Hungarian nuclear power plant, a significant volume of high activity radioactive waste is generated. According to a European Union directive (2011/70/Euratom), all countries that have a nuclear power plant are obliged to solve the management and disposal of the generated radioactive waste. The final disposal of this type of waste in Hungary, as in most countries on Earth, has not yet been resolved, but research has been going on for several decades. Based on a national screening of geological formations, the potential disposal site of high-level radioactive waste in Hungary is the Late Permian Boda Claystone Formation (BCF; Konrád and Hámos, 2006). Due to its significant (>150 km^2) subsurface distribution area and thickness (700–900 m; Máthé, 2015), its low porosity and permeability (Fedor et al., 2008), the BCF has decent insolating properties. However, knowledge of its structural development may be vital in assessing its suitability, as fractures may highly increase the permeability of the rock body, and significant fluid migration may occur along the planes of structural inhomogeneities, as evidenced by mineral-filled fractures, so-called veins. Several authors have studied the veins in the BCF in the last three decades. Árkai et al. (2000) classified the veins from 12 different locations (boreholes and tunnels) into calcite-, barite + quartz- (±calcite and sulfidic mineralisation) and anhydrite-dominated generations. Based on fluid inclusion microthermometry (Török, 1994) and H–C–O stable isotope geochemistry, the barite-quartz-dominated veins formed at ~150 °C from magmatic parent fluid, while the calcite-dominated veins precipitated at ~70 °C from meteoric waters, which, based on δD compositions, are related to warm and cold climates (Árkai et al., 2000). There is no available information about the origin of anhydrite-dominated veins as the amount of carbonate was insufficient for stable isotope analyses. Large data scattering of final melting temperatures (T_m) measured in anhydrite-dominated veins suggests mixing fluids of very different salinity. The lowest T_m data is −17.6 °C which corresponds to a high

* Corresponding author.
E-mail address: ervin.hrabovszki@geo.u-szeged.hu (E. Hrabovszki).

https://doi.org/10.1016/j.jsg.2021.104490
Received 27 January 2021; Received in revised form 5 November 2021; Accepted 27 November 2021
Available online 4 December 2021

salinity solution (20.8% wNaCl$_{eq}$), while the minimal salinity is 7.9% wNaCl$_{eq}$. The observed eutectic temperatures (T_e) between −23.5 and −39.0 °C indicate that the parent fluid of the anhydrite-dominated veins was an H_2O–NaCl–$CaCl_2$ solution (Török, 1994). The calcite-dominated veins precipitated from less saline (2.6–5.6% wNaCl$_{eq}$) aqueous solutions. Lenti et al. (2010) determined homogenization temperature of ~105 °C for inclusions in barite-calcite veins from the tunnel Alfa–1, which veins were precipitated from low salinity (3.2–4.3% wNaCl$_{eq}$) aqueous solutions. Hrabovszki et al. (2017) studied the average dip angle, mineralogical composition, macroscopic- and growth morphologies of veins from the BAF–2 well. The average dip values are 22°, 42°, and 70°, respectively. The vein geometries are straight, branched, en-echelon, and breccia-like. The vein-filling minerals are calcite and anhydrite with a small amount of barite-celestine, albite, pyrite-chalcopyrite, and quartz. The vein growth morphologies are both syn-, anti- and ataxial; however, the vein texture is often complex. In these cases, the mentioned, widely accepted classification of growth morphologies (Ramsay and Huber, 1983; Bons, 2000; Bons et al., 2012) cannot be applied. A well-defined vein type is the branched calcite-barite vein, which, established on microstructural characteristics such as cone-in-cone arrangement of wall rock inclusions within the veins (Vein$_{CIC}$), is suggested to be of early, syn-diagenetic origin (Hrabovszki et al., 2020).

Most of the earlier studies on veins in the BCF focus on the geochemical and mineralogical properties; little attention was paid to microstructures and growth morphologies, and none to the complex interpretation of both. Therefore, in this study, we apply microtextural observations coupled with geochemical techniques to explore the relationships between these properties and provide a new contribution to the existing knowledge about the tectonic evolution and paleofluid history of the BCF. To this end, we interpret together the origin of the fluids, the material transport modes, and the physicochemical conditions of vein formation, since veins are the results of both physical and chemical processes (Bons et al., 2012).

In this paper, we show the petrographic characteristics of four vein generations from the BAF–2 well of the BCF. The homogenization temperatures and final melting temperatures of 7 different vein cement phases are presented. Carbon and oxygen isotopic compositions of vein-forming and wall-rock carbonates, as well as sulphur isotopic compositions of vein-filling sulphates and pyrite are shown. The crystal morphology, vein growth- and material transport mechanisms are discussed together with fluid inclusions and stable isotope compositions. In this way, we reveal new findings about diagenetic processes, the origin of the parent fluids, and potential tectonic events.

2. Geological background

2.1. Regional geology

The study area is located in the Pannonian Basin, Central Europe. The Paleozoic–Mesozoic basement of the Pannonian Basin is built up of two terranes: the ALCAPA Mega-unit (ALCAPA Composite Terrane) and the Tisza Mega-unit (Tisia Terrane; e.g. Haas et al., 2013). The ALCAPA Mega-unit forms the northwestern, while the Tisza Mega-unit forms the southeastern part of the basement. Between these microplates, the Mid-Hungarian Fault Zone divides the pre-Neogene basement in ENE–WSW direction (Fig. 1A). The terranes got juxtaposed during Early Miocene processes (details in Chapter 2.3). Within the Hungarian part of the Tisza Mega-unit, the basement outcrops occur only in the Villány and the Mecsek Mountains (Fig. 1B). The Western Mecsek Mts. Consists of Paleozoic–Triassic sedimentary rocks, including the Late Permian BCF, which contains the veins that are the subjects of the present study (Barabás-Stuhl, 1981). Whether these veins are limited to the BCF or also appear in the under- and overlying formations is an important topic for future research, as this has not been studied by anyone before.

2.2. Lithological characteristics and sedimentary environment

The BCF is a fine-grained clastic sedimentary rock consisting of reddish-brown albitic claystone interbedded with dolomite, siltstone, and sandstone. Another common rock type is albitolite, which contains more than 50 wt% authigenic albite. The BCF gradually overlies the Cserdi Conglomerate Formation. The Kővágószőlős Sandstone Formation overlies the BCF gradually in the southern and central part of the

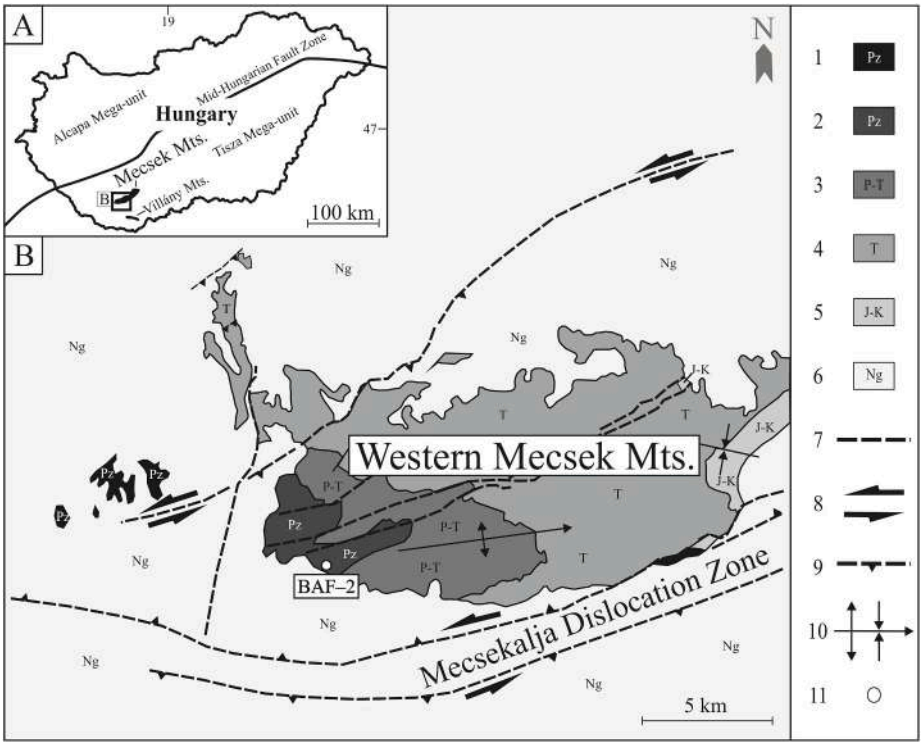

Fig. 1. A–The location of the Western Mecsek Mts. within Hungary. B–Distribution of the Boda Claystone Formation based on Konrád and Sebe (2010). Legend: 1 – Palaeozoic in general; 2 – Boda Claystone Fm; 3 – Late Permian Kővágószőlős Sandstone Fm; 4 – Triassic sediments (sandstones, carbonates, evaporites); 5 – Jurassic and Cretaceous sediments and Cretaceous volcanite; 6 – Neogene sediments; 7 – fault; 8 – strike-slip fault; 9 – thrust fault; 10 – syncline and anticline with the trend of the fold axis; 11 – well site.

Western Mecsek Mts., while with a sharp lithological transition in the northern part (Máthé, 2015). The largest observed sediment thickness in core from the BAF–2 well, drilled in the southern part of the Western Mecsek Mts., is 900 m. However, a continuous record of the sedimentary sequence has not yet been obtained by drilling. The provenance area of the BCF consists of felsic volcanic rocks, metamorphic basement rocks and intermediate–mafic volcanic rocks in small quantities (Varga et al., 2006; Varga, 2009). Quartz, authigenic albite, illite, chlorite, calcite, dolomite and hematite are the dominant rock-forming minerals (Árkai et al., 2000; Máthé, 2015). The crystallinity parameters of the phyllosilicates (IC and ChC values) and the vitrinite reflectance values of coalified particles reveal deep diagenetic to low anchizone conditions (200–250 °C) for the BCF, which was achieved in Late Triassic to Jurassic (K-white mica K–Ar ages; Árkai et al., 2000). Although the total sulphur content of the formation is low (usually <0.02%), Máthé and Nádasi (2017) reported a strong correlation between the amount of total organic carbon (TOC) and sulphides in the BAF–2 well. Petrographic, sedimentological, mineralogical and geochemical properties indicate that the formation is alkaline lake sediment, which was deposited on a periodically drying playa mudflat (Árkai et al., 2000; Varga et al., 2005; Konrád et al., 2010; Máthé, 2015). During evaporative concentration and desiccation stages of lake evolution, displacive hopper halite crystals and halite, anhydrite, and gypsum beds were formed in the unconsolidated groundmass (Máthé and Varga, 2012). These hopper crystals and evaporite beds were replaced by carbonate and feldspar crystals during the diagenetic processes (Máthé and Varga, 2012; Máthé, 2015).

2.3. Tectonic evolution

The study area is located in the SW part of the Tisza Mega-unit, which detached from the European plate during the Penninian rifting in the Middle to Late Jurassic (Csontos and Vörös, 2004). The later tectonic evolution of the Mecsek Mts. is related to the Alpine orogeny (e.g. Horváth et al., 2006; Horváth et al., 2015). The movement of the African plate towards the Eurasian plate triggered the closure of a complex ocean system in the Late Jurassic. This convergence resulted in the complete closure of the Eastern Vardar Ocean between the Tisia and Dacia terranes by the Late Cretaceous. This period was characterised by a significant NW–SE shortening in the Mecsek Mts. resulting in folds with NE–SW-trending fold axes (Benkovics et al., 1997). During the Neogene, because of the ongoing approach of the African plate, the Adriatic continental block was pushed towards Europe, causing extrusion of the Tisia-Dacia terranes from the Dinaric system towards the Carpathian embayment. The extrusion provoked extension above a 'rolling-back' subjecting Carpathian slab (subductible lithosphere of the Magura Ocean) and the formation of the Carpathian arc. The roll-back subduction induced tensional stresses and clockwise rotation in the broader surroundings of the Mecsek. This tectonic phase started in the Early Miocene (~20 Ma; dated rhyolite tuff horizon within syn-rift sediments), and it is called the syn-rift period of the Pannonian Basin. As a result, several tensional, locally transtensional stress fields followed each other (e.g. Fodor et al., 1999; Maros et al., 2004) and in the Mecsek Mts. normal faulting was prevalent (Bergerat and Csontos, 1988; Csontos and Bergerat, 1992). The syn-rift period was followed by a (post-) Sarmatian shortening event, which resulted probably in large-scale folding and thrusting in the Mecsek area (Sebe, 2017). Shortly afterwards, a NW–SE extensional/transtensional tectonic phase took place during the post-rift thermal subsidence of the Basin (Csontos et al., 2002; Maros et al., 2004; Horváth et al., 2006; Sebe, 2017). The last and still active tectonic phase (related to the inversion of the Pannonian Basin) started in the Late Pannonian (~7 Ma, Messinian crisis; Csontos et al., 2002). During this event, the Western Mecsek behaved as a single solid block, no signs of post-Miocene tectonic activity can be found (Konrád et al., 2010).

3. Materials and methods

3.1. Sample collection and preparation

Macroscopic and microscopic observations were carried out on 56 drill core samples collected from the 74–899 m interval of the BAF–2 well, covering more than 90% of the total measured depth (TMD). Polarisation microscopy was used in 30-μm thin sections with an Olympus BX41 microscope and an Olympus DP73 digital microscope camera. Cathodoluminescence (CL) microscopic observations were performed with a Reliotron VII CL instrument mounted on an Olympus BX43 microscope. The operation parameters were 7 kV and 0.7 mA. Fluid inclusion (FI) petrography and microthermometry were carried out in doubly polished thin sections of 80–100-μm thickness using a Linkam MDS600 heating-freezing stage mounted on an Olympus BX41 microscope. Polarisation and CL microscopy, as well as FI microthermometry were carried out at the Department of Mineralogy, Geochemistry and Petrology, University of Szeged. The heating-freezing stage was calibrated at −56.6 °C, 0.0 °C and 374.0 °C using synthetic FIs. Detailed petrographic description of FIs was carried out following the criteria of Goldstein and Reynolds (1994). Homogenization temperatures (T_h) were measured applying stepwise (2 °C) heating, checking all studied inclusions between steps. The final melting temperatures of ice [T_m (Ice)] were determined in the presence of the vapour phase. Both T_h and T_m (Ice) values were determined using the cycling technique of Goldstein and Reynolds (1994). Salinities were calculated from T_m (Ice) data using the empirical equation of Bodnar (1993) and are reported as the mass per cent of NaCl equivalent (% wNaCl$_{eq}$). Artificial stretching of single-phase FIs was performed by stepwise heating up to 290 °C. Eutectic temperatures (T_e) were not determined due to limited inclusion sizes. The area per cent of vapour phases in FIs was determined by analysing 2D microscopic images with ImageJ 1.53 g software. Consequently, these values (although they are calculated in a similar way) cannot be regarded as proper volume fraction (φ_V) equivalents.

Scanning electron microscopy coupled with energy-dispersive X-ray spectrometry was performed using a Hitachi S-4700 field emission scanning electron microscope and a Bruker (Röntec) QX2 energy-dispersive X-ray fluorescence spectrometer at the Faculty of Science and Informatics, University of Szeged. The operating parameters were 15–20 kV and 10 μA.

Drilled vein-forming and host rock calcite samples, as well as drilled sulphate and separated vein-filling sulphide samples were analysed for carbon (n = 22), oxygen (n = 22) and sulphur isotope ratios (n = 8) at the Isotope Climatology and Environmental Research Centre (ICER), Institute for Nuclear Research (ATOMKI), Hungarian Academy of Sciences (MTA) by a Thermo Finnigan DELTA^{plus}XP Isotope Ratio Mass Spectrometer using a Fisons NA1500 NCS Elemental Analyser for the carbon and sulphur measurements, and a Thermal Combustion/Elemental Analyser interface for the oxygen measurements. The results are expressed as $\delta^{13}C$, $\delta^{18}O$ and $\delta^{34}S$ relative to V-PDB, V-SMOW and V-CDT standards, where δ (‰) = $(R_{sample}/R_{standard}\text{-}1)*1000$ and R = $^{13}C/^{12}C$ for $\delta^{13}C$, $^{18}O/^{16}O$ for $\delta^{18}O$ and $^{34}S/^{32}S$ for $\delta^{34}S$. The standard deviation of stable isotope measurements is 0.08, 0.1 and 0.4 or better for $\delta^{13}C$, $\delta^{18}O$ and $\delta^{34}S$.

4. Results

4.1. Wall rock

Based on microscopic observations, the homogeneous, reddish-brown wall rock consists of plagioclase, clay minerals, carbonates, hematite and quartz. The plagioclase appears dominantly as an authigenic component. In some cases, the carbonates associated with feldspars occur as authigenic sparry crystals forming mineral filling of characteristic angular shaped pores in the host rock, similar to that observed by Máthé and Varga (2012) and Máthé (2015). In the rock body of the

BAF–2 well, four vein generations can be distinguished.

4.2. Petrography

Certain parts of the petrographic description of the studied veins from the BAF–2 well have already been published (Hrabovszki et al., 2017, 2020; Tóth et al., 2020). However, previous results have been refined using additional analytical methods and will be presented in this study to better understand the relations between the microtextural and geochemical properties of the veins. The observations made in this chapter (e.g. the sequence of mineral phases) are valid for the entire BAF–2 well, regardless of depth.

4.2.1. Veins with cone-in-cone structures ($Vein_{CIC}$)

Based on the intersection of veins (Fig. 2), the $Vein_{CIC}$, which contains many wall rock inclusions, often arranged as nested concentric cones (cone-in-cone structures; Cobbold et al., 2013), forms the oldest generation. The 1–15 mm thick veins consist of calcite, barite-celestine, albite (±K-feldspar), pyrite-chalcopyrite, chlorite, anhydrite and galena crystals (Figs. 3 and 4). The microscopic morphology of the veins is complex, in most cases classic vein-filling textures (e.g. blocky, elongate blocky or stretched crystals) do not appear. Instead, calcite of mosaic ('jigsaw-puzzle' texture; Lovering, 1972; Dong et al., 1995) crystals (Cal_{MOS}; Fig. 5A), or barite-celestine of acicular crystals (Brt-Cls_{ACC}; Fig. 5B) are frequent. Calcite of subhedral morphology appears around the marginal wall rock inclusions along the vein walls ($Cal_{SHR}1$) and in the pores ($Cal_{SHR}2$). A gradual transition from subhedral to mosaic textures can be observed between the Cal_{MOS} and $Cal_{SHR}2$ phases. From among the above-mentioned calcite phases, only the $Cal_{SHR}1$ shows intense cathodoluminescence (CL), which is its distinctive feature (Fig. 5C). The albite (±K-feldspar) crystals are relatively small (<30 μm), they surround the wall rock inclusions and appear along the vein walls (Fig. 5D). In some cases, the feldspar crystals are enclosed by $Cal_{SHR}1$ grains (Fig. 5C). Next to the albite crystals, flakes of chlorite and pyrite-chalcopyrite (±galena) crystals can be observed in increasing quantity with depth. In some cases, diffuse, poorly crystalline aggregates of iron sulphide can be observed in the albite-K-feldspar-calcite assemblage, composed of curved fibres and platy grains (FeS_{FIB}; Fig. 5E). The albite (±K-feldspar), the chlorite and the pyrite-chalcopyrite crystals form a continuous rim along the vein walls at the deeper parts of the drillhole (Fig. 5F). In these rims, galena crystals of 3–5 μm size are present. The wall rock inclusions or even the vein walls located close to the sulphide crystals are faded relative to the normal, deep reddish-brown colour of the wall rock (Fig. 5G). Barite-celestine crystals appear with pyrite-chalcopyrite (±galena) cubes in the pores of calcite or fill the space with the calcite phase. The textural position of the anhydrite phase is specific, the subhedral crystals (Anh_{SHR}) appear in pores (or fill them completely; Anh_{SF}) of calcite, and their precipitation evidently postdates the formation of the other vein-filling minerals (Fig. 5H). Classical microscopic morphologies are observed only in the calcite phase, which is occasionally fibrous ($Cal_{FIB}1$) in the inner parts of the veins.

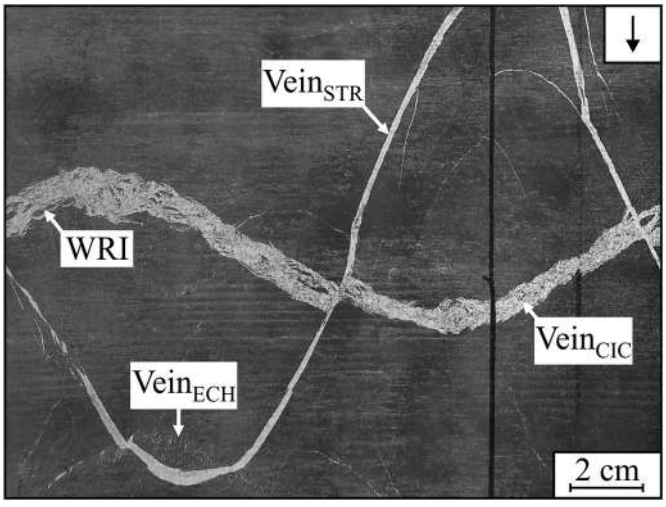

Fig. 2. The mutual relationship of intersecting $Vein_{CIC}$, $Vein_{STR}$ and $Vein_{ECH}$ in a stitched core scanner image, modified after Hrabovszki et al. (2020). The arrow in the upper right corner indicates the down-core direction and the axis of the core sample. WRI–wall rock inclusion.

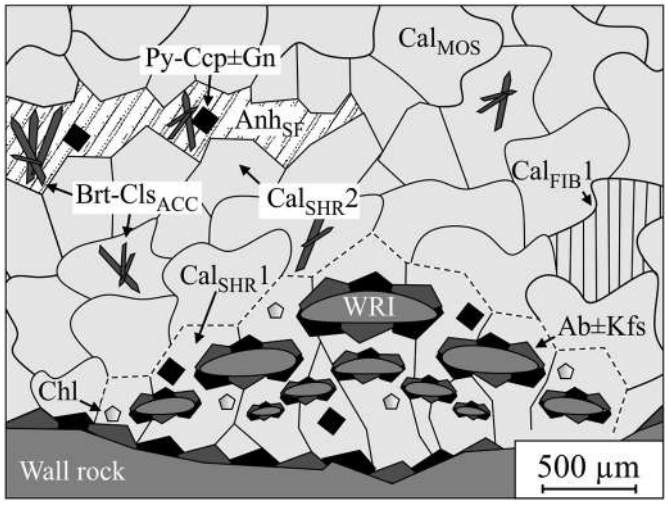

Fig. 3. Schematic representation of minerals and their microtextures in the $Vein_{CIC}$ generation. Ab ± Kfs–albite ± K-feldspar; Chl–chlorite; $Cal_{SHR}1$–subhedral calcite 1; $Cal_{SHR}2$–subhedral calcite 2; $Cal_{FIB}1$–fibrous calcite 1; Cal_{MOS}–calcite of mosaic morphology; Py-Ccp ± Gn–pyrite-chalcopyrite ± galena; Brt-Cls_{ACC}–acicular barite-celestine; And_{SF}–space-filling anhydrite; WRI–wall rock inclusion. The boundary of $Cal_{SHR}1$ is marked out with a white dashed line.

4.2.2. Straight veins ($Vein_{STR}$)

A younger generation of 1–16 mm thick veins whose members intersect the above-mentioned $Vein_{CIC}$ has straight geometry (Fig. 2). These veins show perpendicular opening and parallel shear to the fracture plane (hybrid fractures indicating extensional stress field). The vein-filling minerals are calcite, barite-celestine, anhydrite, and quartz (Fig. 4). The internal structure of these veins can be divided into three parts in which different mineral phases can be observed (Figs. 6 and 7A). In the oldest, 'middle' sector ($Zone_1$) calcite and barite-celestine crystals appear in elongate blocky texture ($Cal_{EB}1A$; Brt-Cls_{EB}; Fig. 7B), the crystals grew out from one wall towards the other. The 'bottom' sector ($Zone_2$) consists mainly of elongate blocky calcite ($Cal_{EB}1B$) and anhydrite crystals (Anh_{EB}), which have also grown in one direction, but now not from the wall rock; they instead grow from the crystals of $Zone_1$ towards the vein wall (Fig. 7C). Next to the anhydrite crystals, fine-grained calcite is frequent along the vein-wall rock boundary. The third and youngest, 'upper' sector ($Zone_3$) is built up by elongate blocky calcite crystals ($Cal_{EB}1C$) and along the vein walls sporadically by fine-grained quartz (Qtz_{FG}). The calcite crystals grew out from the crystals of $Zone_1$ towards the wall rock, but in the opposite direction than the crystals of $Zone_1$ and $Zone_2$. The orange CL colour of the $Zone_3$ calcite is more intense than observed on the crystals of the other zones (Fig. 7B). Between the zones 'seed grains' separated from the wall rock can be observed.

4.2.3. En-echelon vein arrays ($Vein_{ECH}$)

The members of the third vein generation consist of en-echelon vein arrays. The width of these shear zones is between 1 and 4 mm, and they

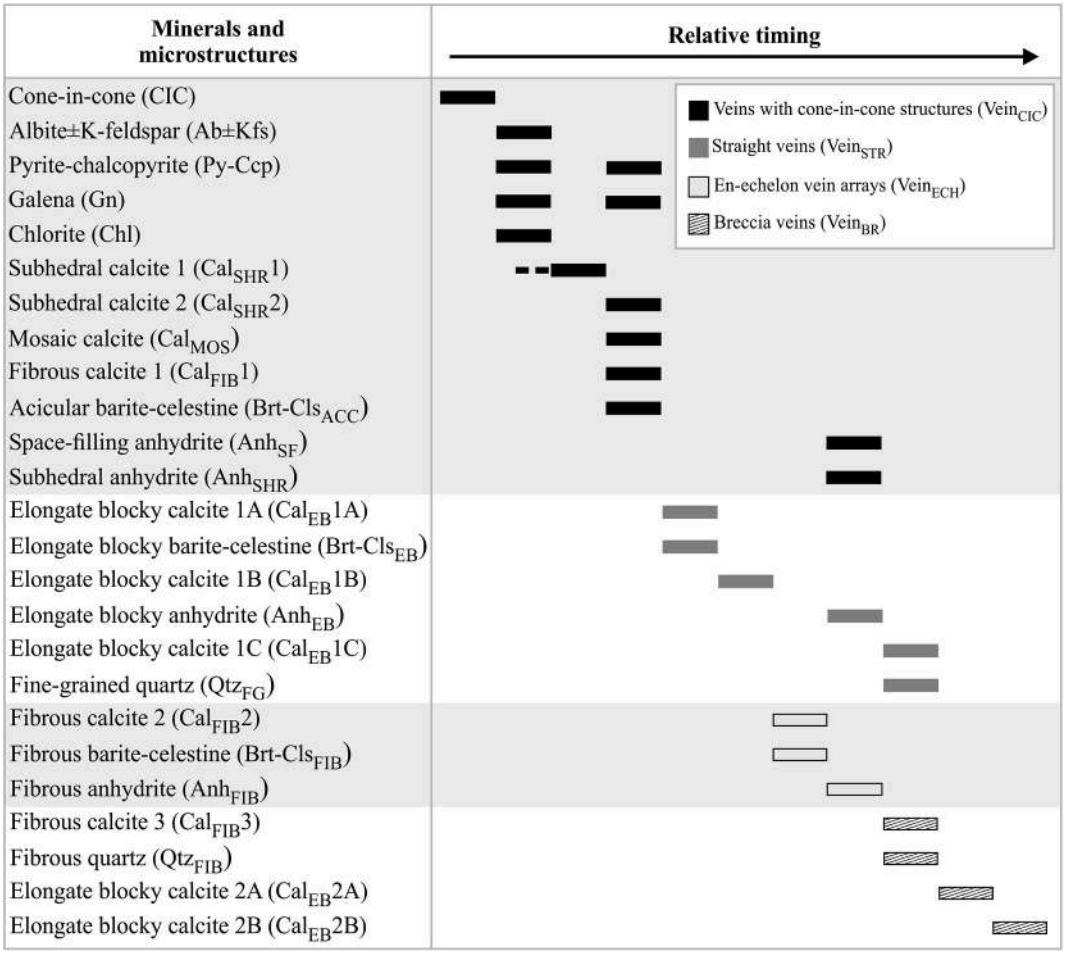

Fig. 4. Paragenetic sequence of the observed microstructures and vein-filling minerals in the BCF (BAF–2 well) indicating the material and fluid transport modes.

shear the straight veins (Vein$_{STR}$) indicating a compressional stress field (Fig. 2). The individual veins are often sigmoidal in shape. The vein-filling crystals are fibrous calcite (Cal$_{FIB}$2), barite-celestine (Brt-Cls$_{FIB}$) and anhydrite (Anh$_{FIB}$; Figs. 4, 8 and 9). The fibrous crystals are occasionally curved and grew out from a median zone consisting of wall rock inclusions. The anhydrite phase is less textured than the other Vein$_{ECH}$-forming minerals, and in many cases contains crystals of the Cal$_{FIB}$2 phase (Fig. 9B).

4.2.4. *Breccia or net veins (Vein$_{BR}$)*

The fourth generation of fracture-fillings is made up of breccia veins. No intersection with other veins can be observed, and no traces of shear can be detected along the Vein$_{BR}$ cannot be detected. These 1–15 mm thick veins contain many angular wall rock inclusions (Figs. 10 and 11A). The main fracture-filling mineral is calcite, whose elongate blocky crystals grew from both vein walls towards the central part of the fractures (Cal$_{EB}$2; Fig. 11B). Based on macroscopic colour, the elongate blocky calcite phase can be divided into two subgroups: a pale reddish (Cal$_{EB}$2A) and a white (Cal$_{EB}$2B) calcite phase, respectively. The Cal$_{EB}$2A crystals cement the wall rock inclusions, while the Cal$_{EB}$2B crystals appear dominantly in pores with aperture sizes up to 10 mm. The relative position of the Cal$_{EB}$2A and B phases can be observed on PPL images, where the Cal$_{EB}$2B phase is more translucent in plane polarised light (Fig. 11C). The cause of this phenomenon and the reddish macroscopic colour is the high amount of hematite flakes and other rock-forming components in the Cal$_{EB}$2A crystals derived from the wall rock. Within the Cal$_{EB}$2A phase microveins of fibrous calcite (Cal$_{FIB}$3) and quartz (Qtz$_{FIB}$) appear in small quantities (Fig. 11D). The three calcite phases have uniform CL characteristics (Fig. 11C and D). It is essential to highlight that no anhydrite overprint occurs on this vein generation.

4.3. *Fluid inclusion microthermometry*

Microthermometric analyses were carried out on all calcite phases, containing measurable assemblages of fluid inclusions (FIAs). Although secondary FIAs appeared in several phases, measurements were performed only on primary or pseudosecondary inclusions, since our main goal was to determine the precipitation conditions of the individual phases. On the other hand, petrographic and microthermometric studies of secondary FIAs may facilitate the future research, as they may represent a late-stage fluid that is closer in composition to the present fluid in the system. As a result, 166 T_h and 82 T_m (Ice) data were obtained from 7 different vein cement phases (Table 1). According to phase transitions, all FIs compose of aqueous solutions with variable salinity. At room temperature, most of the inclusions consist of two phases: liquid (L) + vapour (V) with the domination of the L phase. The area per cent of the V phase is predominantly between 10 and 20 area%. The term "typical values" is used for the fluid inclusion phase transition temperatures ranging from the first (Q1 at 25%) to the third quartile (Q3 at 75%) of the measured data (interquartile range, IQR), which gives a reasonable constraint on the uncertainty associated with the temperature of fluid migration events (Fall and Bodnar, 2018).

The Cal$_{SHR}$2 phase of Vein$_{CIC}$ contains assemblages of FIs arranged parallel to crystal faces (Fig. 12A) suggesting their primary origin. The size of the inclusions' longest dimension varies between 2 and 8 μm. The shapes are usually rounded, occasionally elongate forms can be observed. The T_h(LV→L) of the inclusions varies between 90 and 140 °C

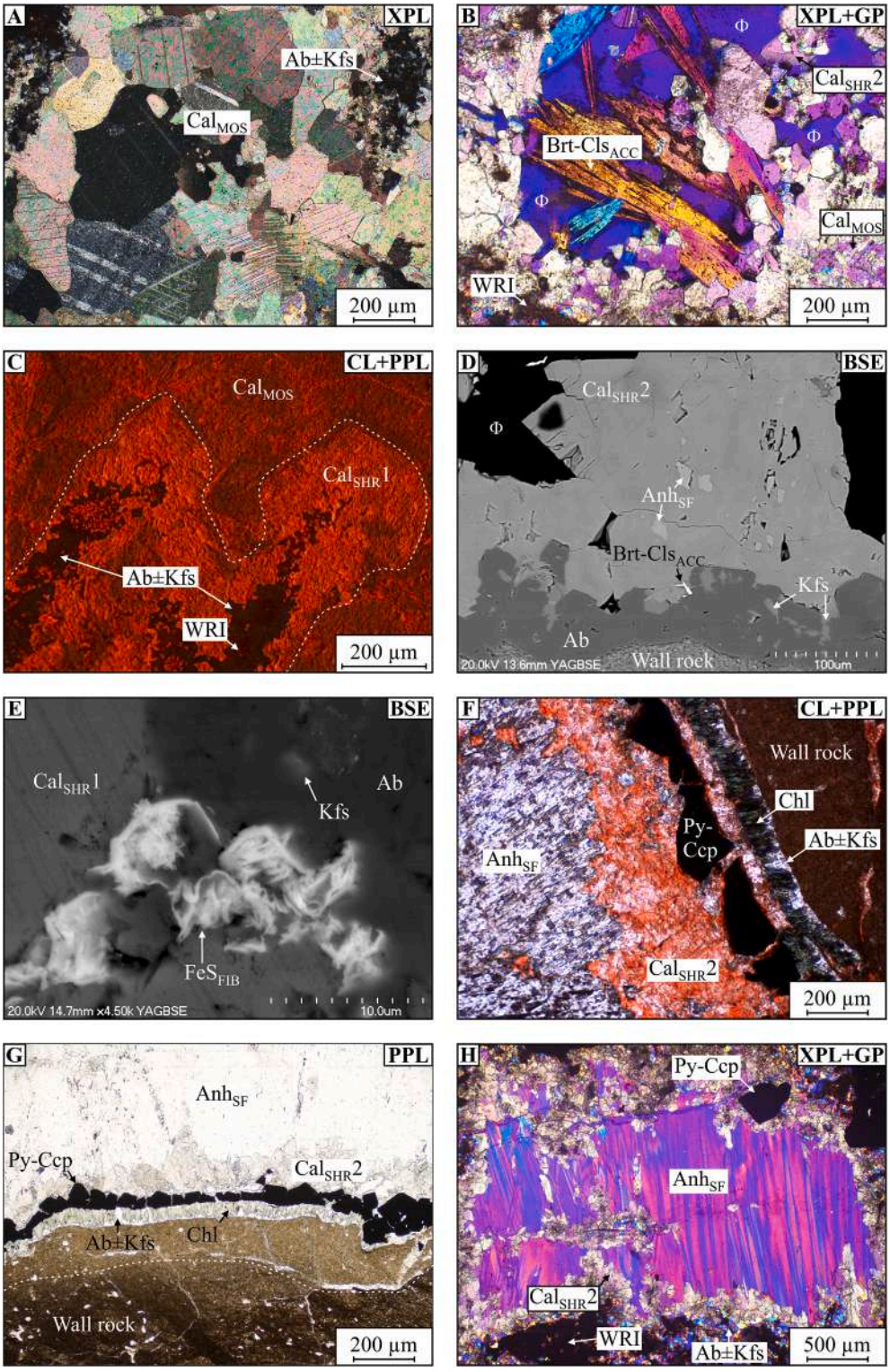

Fig. 5. Minerals and their microtextures in the Vein$_{CIC}$ generation. (A) Mosaic calcite (Cal$_{MOS}$) with interpenetrating grain boundaries in which fine-grained albite ± K-feldspar (Ab ± Kfs) appears around wall rock inclusions. (B) Barite-celestine of acicular habit (Brt-Cls$_{ACC}$) and subhedral calcite (Cal$_{SHR}$2) within pores (Φ) in the Cal$_{MOS}$ phase. Wall rock inclusions (WRI) can be observed near the pores. (C) Subhedral calcite with intense CL colour (Cal$_{SHR1}$, marked out with a white dashed line) around albite ± K-feldspar grains cemented by Cal$_{MOS}$. (D) Albite ± K-feldspar rim around the vein wall followed by subhedral calcite (Cal$_{SHR}$2) and acicular barite-celestine. The pores of Cal$_{SHR}$2 are partially cemented by space-filling anhydrite (Anh$_{SF}$). (E) Fibrous iron sulphide (FeS$_{FIB}$) surrounded by Ab, Kfs and Cal$_{SHR}$1. (F) Rim along the vein-wall rock contact made up of chlorite (Chl), albite ± K-feldspar and pyrite-chalcopyrite (Py-Ccp) crystals. Subhedral calcite can also be observed between these minerals, in the inner parts with pores filled by space-filling anhydrite. (G) Faded wall rock located close to Py-Ccp crystals. The normal, reddish-brown, and faded wall rock boundary is marked with a white dashed line. (H) Anh$_{SF}$ cementing the remnants and pores of different mineral phases. BSE–backscattered electrons; CL–cathodoluminescence; GP–gypsum plate; PPL–plane polarised light; XPL–crossed polarised light. (For interpretation of the references to colour in this figure legend, the reader is referred to the Web version of this article.)

($n = 28$; Fig. 13A), while the typical values T_m (Ice) range between −9.4 and −9.8 °C ($n = 12$; Fig. 13B).

The Cal$_{EB}$1A, Cal$_{EB}$1B and Cal$_{EB}$1C phases of Vein$_{STR}$ contain assemblages of FIs arranged perpendicular to the boundaries of the elongate blocky crystals (Fig. 12B). These planes of FIs can be interpreted as inclusion bands related to crack-sealing (Ramsay, 1980; English and Laubach, 2017), which indicates the primary origin of the FIs. The size of the inclusions' longest dimension varies between 2 and 7 µm. Their shape is mainly irregular, less commonly rounded, or elongate. The T_h(LV→L) of the inclusions in Cal$_{EB}$1A ranges from 80 to 144 °C ($n = 19$; Fig. 13A), and the T_m (Ice) varies dominantly between −3.1 and −6.4 °C ($n = 9$; Fig. 13B). In the Cal$_{EB}$1B phase, the T_h(LV→L) values are in the range of 94 and 132 °C ($n = 35$; Fig. 13A), the T_m (Ice) of the inclusions varies predominantly between −2.8 and −6.2 °C ($n = 11$; Fig. 13B). FIs of Cal$_{EB}$1C have T_h(LV→L) values ranging from 84 to 142 °C ($n = 22$; Fig. 13A), and typical T_m (Ice) values ranging from −3.6 to −5.9 °C ($n = 13$; Fig. 14B).

The fibrous calcite crystals (Cal$_{FIB}$2) of the Vein$_{ECH}$ contain two-

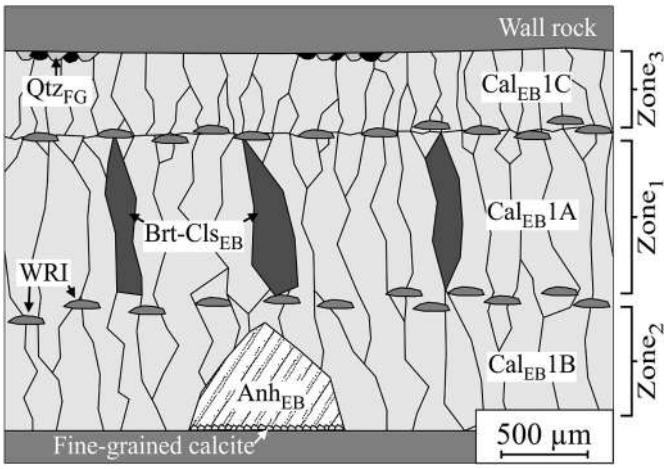

Fig. 6. Schematic representation of minerals and their microtextures in the Vein$_{STR}$ generation. Cal$_{EB}$1A–elongate blocky calcite 1 A; Brt-Cls$_{EB}$–elongate blocky barite-celestine; Cal$_{EB}$1B–elongate blocky calcite 1 B; Anh$_{EB}$–elongate blocky anhydrite; Cal$_{EB}$1C–elongate blocky calcite 1C; Qtz$_{FG}$–fine-grained quartz; WRI–wall rock inclusion. The white arrow indicates the fine-grained calcite phase.

phase FIs along planes that do not cross grain boundaries (Fig. 12C) suggesting the pseudosecondary or primary origin of the inclusions. The shapes are usually oval and elongate varying between 2 and 12 µm maximum sizes. The T_h(LV→L) values are between 80 and 135 °C (n = 29; Figs. 13E and 14A), and the T_m (Ice) range dominantly from −3.4 to −4.6 °C (n = 12; Fig. 13B).

Within the Vein$_{BR}$-type fracture fillings, only the Cal$_{EB}$2A phase contains two-phase (L + V) FIs, while the Cal$_{EB}$2B phase contains one-phase (L) inclusions dominantly. The elongate to irregular shaped primary FIs in the calcite crystals are common in planes parallel to grain boundaries (Fig. 12D). The maximum inclusion sizes in the Cal$_{EB}$2A are between 2 and 10 µm, while those in the Cal$_{EB}$2B are between 6 and 27 µm. T_h(LV→L) values of Cal$_{EB}$2A are between 130 and 164 °C (n = 30; Fig. 13A), and the T_m (Ice) varies dominantly between −2.1 and −2.6 °C (n = 12; Fig. 13B). In the Cal$_{EB}$2B phase, only three two-phase inclusions could be measured, the T_h(LV→L) values are between 43 and 50 °C. After T_h measurements, the artificial stretching of the FIs allowed the determination of several T_m (Ice) data ranging dominantly from 0.0 to −0.2 °C (n = 13).

4.4. Stable isotope compositions

The carbon and oxygen isotopic compositions were measured in vein-forming and wall-rock carbonates (Fig. 14, Table 2). The Cal$_{SHR}$2 phase of the Vein$_{CIC}$ displays a narrow range of $\delta^{13}C$ values between −5.43 and −3.81‰ and $\delta^{18}O$ values between 16.57 and 18.39‰ regardless of total measured depth. These values are relatively consistent with the $\delta^{18}O$ composition of the calcite phases of Vein$_{STR}$ (Cal$_{EB}$1A, -B and –C) between 14.63 and 17.31‰ and the $\delta^{13}C$ composition between −5.23 and −3.98‰. The calcite phase of the Vein$_{ECH}$ (Cal$_{FIB}$2) has $\delta^{13}C$ composition between −4.08 and −3.36‰ and $\delta^{18}O$ composition between 19.05 and 19.34‰. These values are close to those typical of most of the wall rock carbonate samples (Cb$_{WR}$). The calcite phases of the Vein$_{BR}$ (Cal$_{EB}$2A and Cal$_{EB}$2B) have various $\delta^{13}C$ and $\delta^{18}O$ compositions; however, these values are also not far from the values of other veins.

Determination of sulphur isotopic composition was carried out on vein-filling sulphates (anhydrite, barite-celestine) and pyrite (Fig. 15, Table 3). The $\delta^{34}S$ composition of all the anhydrite phases (Anh$_{SF}$; Anh$_{EB}$ and Anh$_{FIB}$) falls in a narrow interval between 4.14 and 7.35‰. The $\delta^{34}S$ composition of barite-celestine phases (Brt-Cls$_{ACC}$ and Brt-Cls$_{EB}$) are the most enriched in ^{34}S with values between 12.00 and 13.88‰. The $\delta^{34}S$ composition of the BAF–2_831/2 pyrite sample is similar to the $\delta^{34}S$ values of wall rock and vein-filling pyrite (ranging from −4.30 to 5.90‰) from the BAF–2 well observed by Máthé and Nádasi (2017);

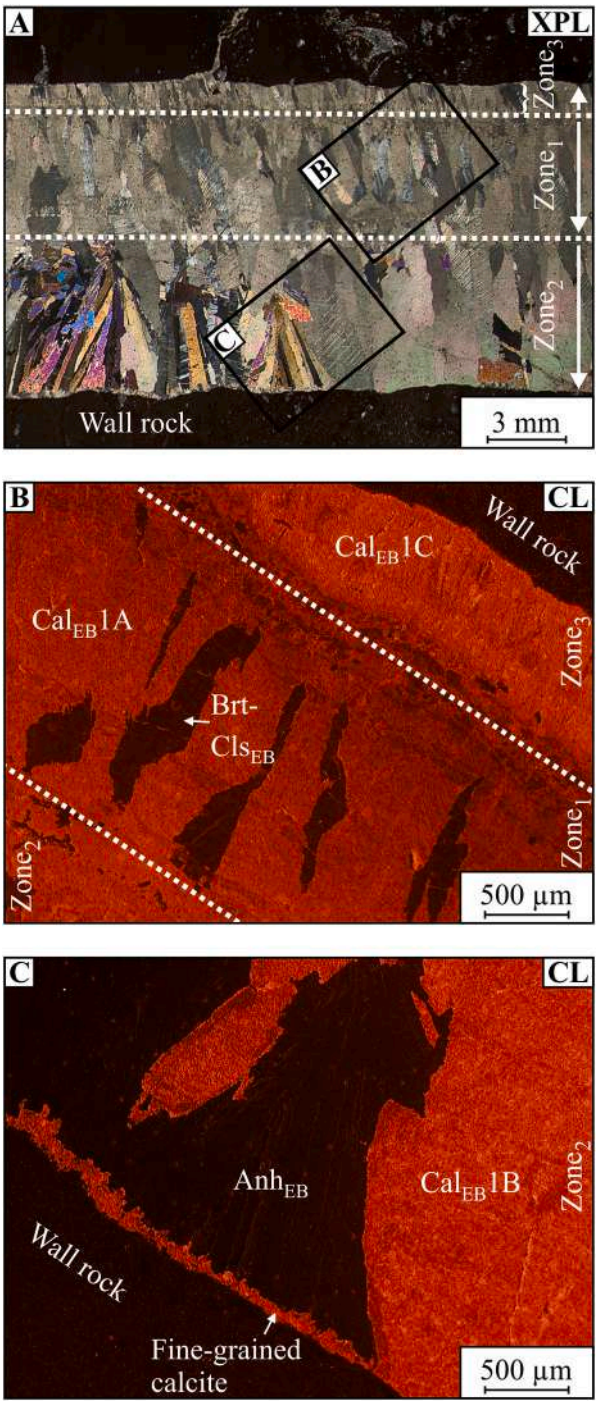

Fig. 7. Minerals and their microtextures in the Vein$_{STR}$ generation. (A) Three zones of different mineralogical compositions are observed. (B) The 'middle zone' (Zone$_1$) consists of elongate blocky calcite (Cal$_{EB}$1A) and barite-celestine (Brt-Cls$_{EB}$). The 'upper zone' (Zone$_3$) consists of intense orange CL elongate blocky calcite (Cal$_{EB}$1C). (C) The 'bottom zone' (Zone$_2$) consists of elongate blocky calcite (Cal$_{EB}$1B) and anhydrite (Anh$_{EB}$). Along the vein-wall rock boundary, fine-grained calcite is frequent next to the anhydrite crystals. CL–cathodoluminescence; XPL–crossed polarised light. (For interpretation of the references to colour in this figure legend, the reader is referred to the Web version of this article.)

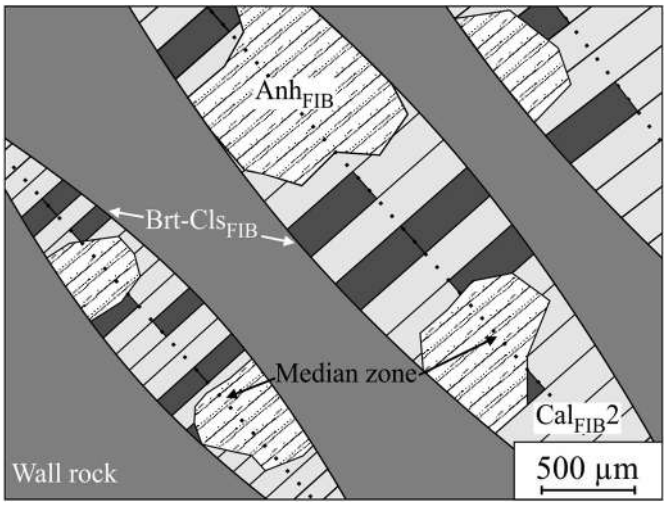

Fig. 8. Schematic representation of minerals and their microtextures in the Vein$_{ECH}$ generation. Cal$_{FIB}$2–fibrous calcite 2; Brt-Cls$_{FIB}$–fibrous barite-celestine; Anh$_{FIB}$–fibrous anhydrite.

however, the BAF–2_622/2 pyrite sample has an extremely depleted $\delta^{34}S$ value of −18.01‰.

5. Discussion

5.1. Crystal morphology, vein growth- and material transport mechanisms

5.1.1. Veins with cone-in-cone structures (Vein$_{CIC}$)

The Vein$_{CIC}$ generation contains polytextured veins, which have a variety of textures, including fibrous and subhedral crystals, of seven different mineral phases, indicating sequential vein development (Bons, 2000). Moreover, the interpretation of crystal morphologies should be consistent with the vein-formation mechanism suggested by the microstructure (wall rock inclusions; WRIs) of the veins.

The albite ± K-feldspar (Ab ± Kfs) crystals (±chlorite ± pyrite ± chalcopyrite ± galena) may have formed during the diagenetic alteration of the BCF (Árkai et al., 2000; Varga et al., 2005) after the antitaxial growth of the veins (Hrabovszki et al., 2020). In general, during albitisation, the detrital K-felspar or calcic plagioclase is replaced by pure (>99 mol%) albite (Boles, 1982; Burley and Worden, 2003). As part of the process, Ca^{2+} from the detrital feldspar can react with the HCO_3^--content of the pore fluid forming calcite cement. The diagenetic origin of the vein-forming Ab ± Kfs phase is supported by the lack of twins and CL activity of the crystals (Fig. 5C, F) which are characteristics of diagenetic feldspars (Kastner and Waldbaum, 1968; Kastner, 1971; Kastner and Siever, 1979; Saigal et al., 1988). Around Ab ± Kfs, the subhedral morphology of the calcite crystals (Cal$_{SHR}$1 and Cal$_{SHR}$2; Fig. 5C and D) indicates, that fluids migrated around these minerals during their growth. Based on the mosaic morphology (Lovering, 1972; Dong et al., 1995) of Cal$_{MOS}$, the gradual transition from subhedral to mosaic texture, and uniform CL characteristics, the Cal$_{MOS}$ can be interpreted as the recrystallised form of the Cal$_{SHR}$2 phase.

The interpretation of Cal$_{FIB}$1 is established on the following: Based on the geometries and unique arrangements of WRIs, Hrabovszki et al. (2020) suggested that the mechanism of Vein$_{CIC}$ formation was continuous. Continuous vein formation would result in fibrous crystals (Means and Li, 2001; Wiltschko and Morse, 2001; Hilgers and Urai, 2005); therefore, the original texture of the Vein$_{CIC}$ was most probably fibrous, consisting of evaporite minerals (Hrabovszki et al., 2020). Since Cal$_{FIB}$1 is part of the Cal$_{SHR}$2-Cal$_{MOS}$-Cal$_{FIB}$1 assemblage, which is evidently younger, than the Ab ± Kfs-Chl-Py-Ccp-Gn-Cal$_{SHR}$1 one, it probably represents a relict microstructure of the original fibrous filling of the antitaxial veins.

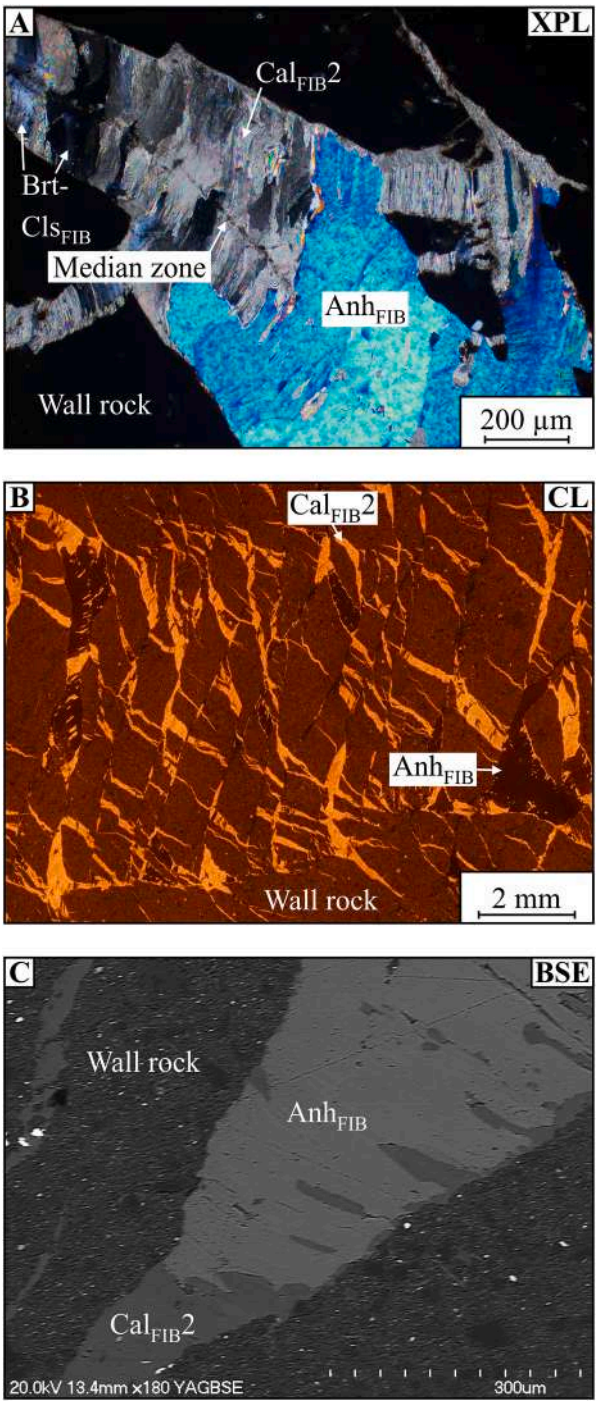

Fig. 9. Minerals and their microtextures in the Vein$_{ECH}$ generation. (A) The en-echelon veins consist of fibrous calcite (Cal$_{FIB}$2), barite-celestine (Brt-Cls$_{FIB}$) and anhydrite (Anh$_{FIB}$). (B and C) Fibrous calcite crystals are surrounded by the anhydrite phase. BSE–backscattered electrons; CL–cathodoluminescence; XPL–crossed polarised light.

According to these observations, the Vein$_{CIC}$ fractures cemented in the following stages: (1) Ab ± Kfs crystals (±chlorite flakes, ±pyrite-chalcopyrite, ±galena) precipitated around WRIs and along vein walls. (2) In some cases, Cal$_{SHR}$1 crystals grew on Ab ± Kfs. (3) Cal$_{SHR}$2 and Cal$_{FIB}$1 associated with Brt-Cls$_{ACC}$ (±pyrite-chalcopyrite and galena; Fig. 5B, D, H) precipitated on Cal$_{SHR}$1 crystals (visible only in cathodoluminescence images; Fig. 5C). (4) Parts of the Cal$_{SHR}$2 phase recrystallised forming mosaic texture (Cal$_{MOS}$). (5) The remaining pores and cavities of the veins were filled by space-filling and subhedral

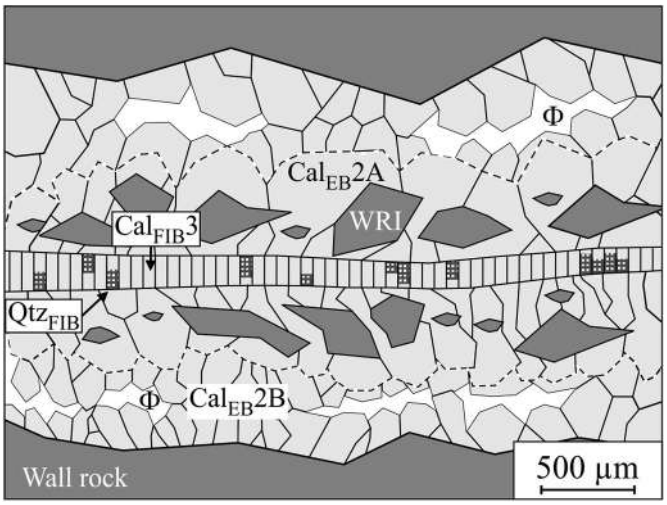

Fig. 10. Schematic representation of minerals and their microtextures in the Vein$_{BR}$ generation. Cal$_{FIB}$3–fibrous calcite 3; Qtz$_{FIB}$–fibrous quartz; Cal$_{EB}$2A-–elongate blocky calcite 2 A; Cal$_{EB}$2B–elongate blocky calcite 2 B; Φ–pore; WRI–wall rock inclusion. The boundary of Cal$_{EB}$2A is marked out with a white dashed line.

anhydrite crystals (Anh$_{SF}$ and Anh$_{SHR}$; Fig. 5D, H). Since the minerals in Vein$_{CIC}$ cannot be classified by the classic blocky, elongate blocky or stretched textures and the amount of fibrous crystals is insignificant, the categorisation of the vein growth mechanism to the standard types (e.g. syntaxial, antitaxial or ataxial; Bons et al., 2012) is problematic. On the other hand, some findings can be made about fluid migration: The close contact of the Ab ± Kfs and the wall rock suggests that parts of the Ab ± Kfs forming components originate from the wall rock. The subhedral crystal faces of the Cal$_{SHR}$1 indicate the opportunity of an advective fluid transport in the voids and cavities of the veins. This kind of advection could also be the transport mode of the parent fluids of the Cal$_{SHR}$2, and syngenetic Brt-Cls$_{ACC}$ (±Py-Ccps) as well as of the finally precipitated Anh$_{SF}$ and Anh$_{SHR}$ phases.

5.1.2. *Straight veins (Vein$_{STR}$)*

The straight veins consist of elongate blocky calcite (Cal$_{EB}$1A, B and C), barite-celestine (Brt-Cls$_{EB}$), anhydrite (Anh$_{EB}$), fine-grained calcite and quartz (Qtz$_{FG}$) phases (Fig. 7). The elongate blocky crystal shape is characteristic of syntaxial veins (Bons, 2000). The three zones of different mineral compositions are the results of (at least) three major (and numerous minor) crack-seal events. Between the zones, planes of solid inclusions can be interpreted as inclusion bands (Ramsay, 1980; Koehn and Passchier, 2000) separated from the wall during subsequent cracking events. After forming the first fracture, crystals of Cal$_{EB}$1A and Brt-Cls$_{EB}$ grew from one side of the wall rock towards the other. The second crack developed on that side of the vein where the wider, and therefore the younger, parts of the crystals were located (Bons et al., 2012). This crack filled with Cal$_{EB}$1B, which was replaced later by Anh$_{EB}$. The third opening occurred at the Cal$_{EB}$1-wall rock contact. It was sealed by the crystals of Cal$_{EB}$1C and fine-grained quartz (Qtz$_{FG}$). Generally, the vein development can be interpreted as the result of separated cracking and 'one-sided' sealing events; accordingly, the members of Vein$_{STR}$ are syntaxial veins composed of unitaxial parts (Hilgers et al., 2001). The elongate blocky grains indicate that the transport mode was advective, the parent fluids of the minerals flowed through open fractures, which allowed intense crystal growth competition. Fracturing, advective fluid flow, and sealing happened at least in three major stages, with fluid composition changes over time.

5.1.3. *En-echelon vein arrays (Vein$_{ECH}$)*

The veins of Vein$_{ECH}$ consist of fibrous calcite (Cal$_{FIB}$2), barite-

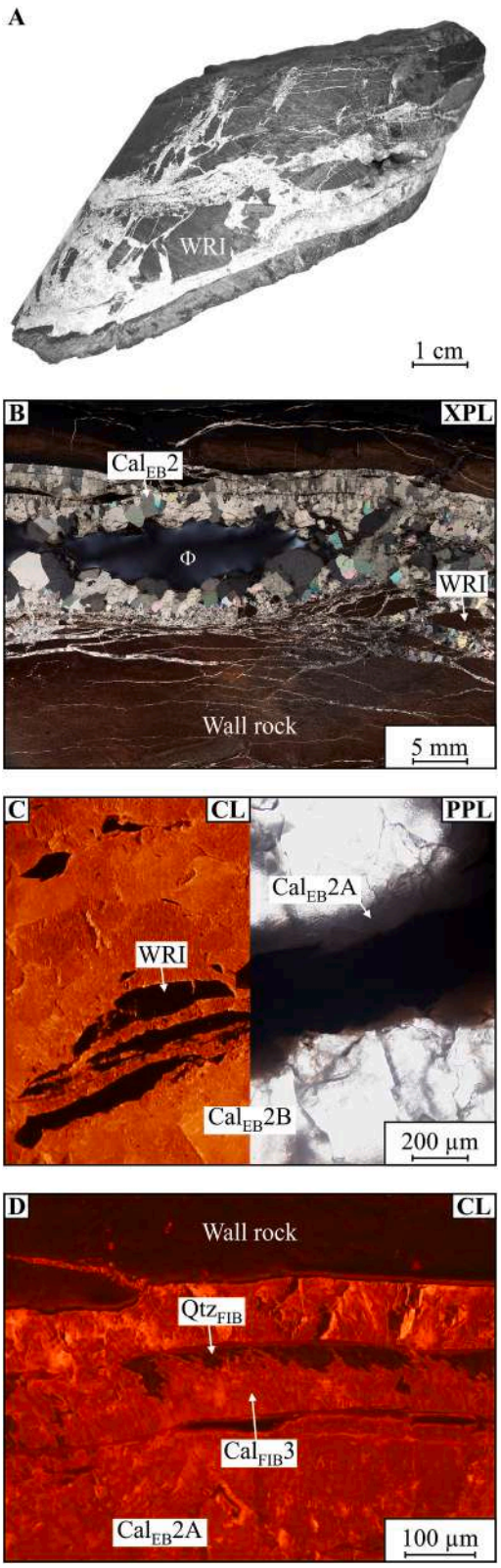

Fig. 11. Structure, microtexture, and fracture-filling minerals of the Vein$_{BR}$ generation. (A) Angular wall rock inclusions (WRI) of cm size are frequent in the mineral matrix. (B) The main vein-forming mineral is calcite of elongate blocky morphology (Cal$_{EB}$2). (C) Cal$_{EB}$2A and Cal$_{EB}$2B subgroups of the elongate blocky calcite phase. (D) Amongst the Cal$_{EB}$2A crystals zones of fibrous quartz (Qtz and calcite (Cal$_{FIB}$3) are also observed. CL–cathodoluminescence; PPL–plane polarised light; XPL–crossed polarised light.

Table 1
First (Q1) and third quartile (Q3) of T_h and T_m (Ice) measured from 7 different calcite phases. *n*–number of measurements.

Vein type	Mineral phase	T_h (°C)		*n*	T_m (Ice; °C)		*n*
		Q1	Q3		Q1	Q3	
$Vein_{CIC}$	$Cal_{SHR}2$	109	130	28	−9.8	−9.4	12
$Vein_{STR}$	$Cal_{EB}1A$	108	128	19	−6.4	−3.1	9
	$Cal_{EB}1B$	112	128	35	−6.2	−2.8	11
	$Cal_{EB}1C$	122	132	22	−5.9	−3.6	13
$Vein_{ECH}$	$Cal_{FIB}2$	99	115	29	−4.6	−3.4	12
$Vein_{BR}$	$Cal_{EB}2A$	140	148	30	−2.6	−2.1	12
	$Cal_{EB}2B$	43	50	3	−0.2	0.0	13

celestine (Brt-Cls_{FIB}) and anhydrite (Anh_{FIB}). The fibrous texture and the median zone of the veins (Fig. 9A) suggest their antitaxial growth. Keeping in mind that the observed en-echelon veins appear in shear zones, it is likely that their opening was passive (Hilgers and Urai, 2005), i.e. the fracturing and vein widening were controlled by the progression of the shear zones and not by the pressure generated by the growing crystals (P_{fc}; Means and Li, 2001; Wiltschko and Morse, 2001). The growth direction of the optically undeformed, curved fibrous crystals (showing no or little growth competition) followed the vein walls tracking at least partly the opening trajectory (Urai et al., 1991) of the veins. The anhydrite phase is less textured than the $Cal_{FIB}2$ and Brt-Cls_{FIB}, it contains remnants of $Cal_{FIB}2$ (Fig. 9B and C), and within the anhydrite domains, the presence of the median zone is subordinate (Fig. 9A). Based on these observations, the Anh_{FIB} is not a primary vein-forming mineral phase, preferably it replaced the original, finely textured $Cal_{FIB}2$ and Brt-Cls_{FIB} phases. Since the members of $Vein_{ECH}$ are antitaxial veins, it can be stated that they did not function as advective flow paths (Bons et al., 2012). On the other hand, the material transport mechanism related to vein formation could be either advective (pervasive flow through the pore network of the wall rock), or, considering that the evolution of the shear zones took place in a lithified low porosity-permeability claystone (Tóth et al., 2020), more likely diffusive (Bons et al., 2012).

5.1.4. Breccia or net veins ($Vein_{BR}$)

The formation of the $Vein_{BR}$ can be interpreted as a result of the following processes: (1) Calcite ($Cal_{FIB}3$) and quartz (Qtz_{FIB}) precipitated along weakness planes of the claystone (e.g. bedding planes) forming antitaxial veins. Neither active nor passive vein widening can be excluded. Nevertheless, an acceptable explanation is that the increased fluid pressure (P_f) and elevated supersaturation in the pore fluid induced the development of actively opening (displacive; Taber, 1916; Woodland, 1964; Franks, 1969; Hilgers and Urai, 2005) fibrous veins due to the pressure exerted by crystallisation (P_{fc}) (Hrabovszki et al., 2020). In this case, advection was not required, since diffusion could be the primary material transport even in the case of stagnant fluids (Bons, 2000). (2) Due to the further increase in P_f, fractures opened along the fibrous veins, which served as weakness planes (Sibson and Scott, 1998). Elongate blocky calcite crystals ($Cal_{EB}2A$) cemented the fragments of the fibrous veinlets and the newly formed wall rock inclusions. Based on the angular WRIs which can be fitted together and to the vein walls (Fig. 11A and B), this event can be interpreted as hydraulic fracturing, which occurred in the well-lithified state of the BCF. The parent fluid of the $Cal_{EB}2A$ could flow with the propagating fractures (mobile hydrofractures; Bons, 2001). (3) Elongate blocky calcite crystals ($Cal_{EB}2B$) precipitated on the $Cal_{EB}2A$ phase from a fluid which migrated within the remaining pores and cavities of the veins. Consequently, these veins, similar to $Vein_{CIC}$, are partially filled polytextured veins in which an initial antitaxial growth was followed by syntaxial vein development. The observed heterogeneity in vein growth morphology also indicates a change in the mode of opening mechanisms and nature of fluid migration.

5.2. Fluid inclusions and stable isotope compositions

In the $Vein_{CIC}$ and $Vein_{SRT}$ generations, the T_h values of the carbonate phases ($Cal_{SHR}2$, $Cal_{EB}1A$-B-C) are in close range (typical values are between 108 and 132 °C; Figs. 12, 13 and 17). The T_h values measured in $Vein_{ECH}$ ($Cal_{FIB}2$) are close to those of the $Vein_{CIC}$ and $Vein_{STR}$ generations; however, a slight decrease can be observed (typical values range from 99 to 115 °C; Figs. 12, 13 and 17). In contrast, T_h values of the

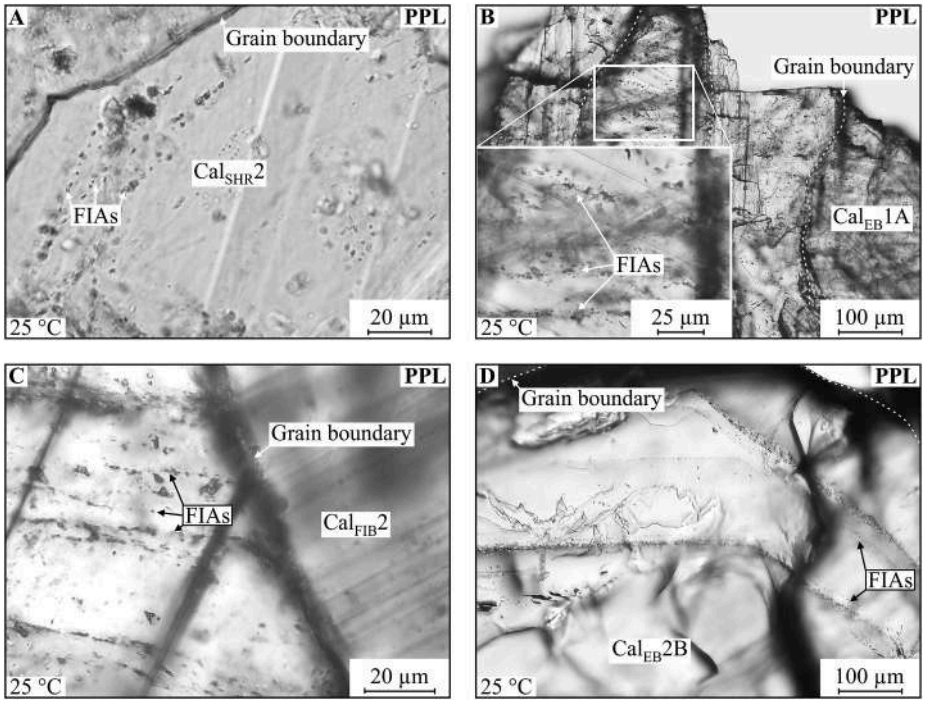

Fig. 12. Fluid inclusion assemblages (FIAs) within the $Cal_{SHR}2$ (A), $Cal_{EB}1A$ (B), $Cal_{FIB}2$ (C) and $Cal_{EB}2B$ (D) mineral phases of the $Vein_{CIC}$, $Vein_{STR}$, $Vein_{ECH}$ and $Vein_{BR}$. PPL–plane-polarised light.

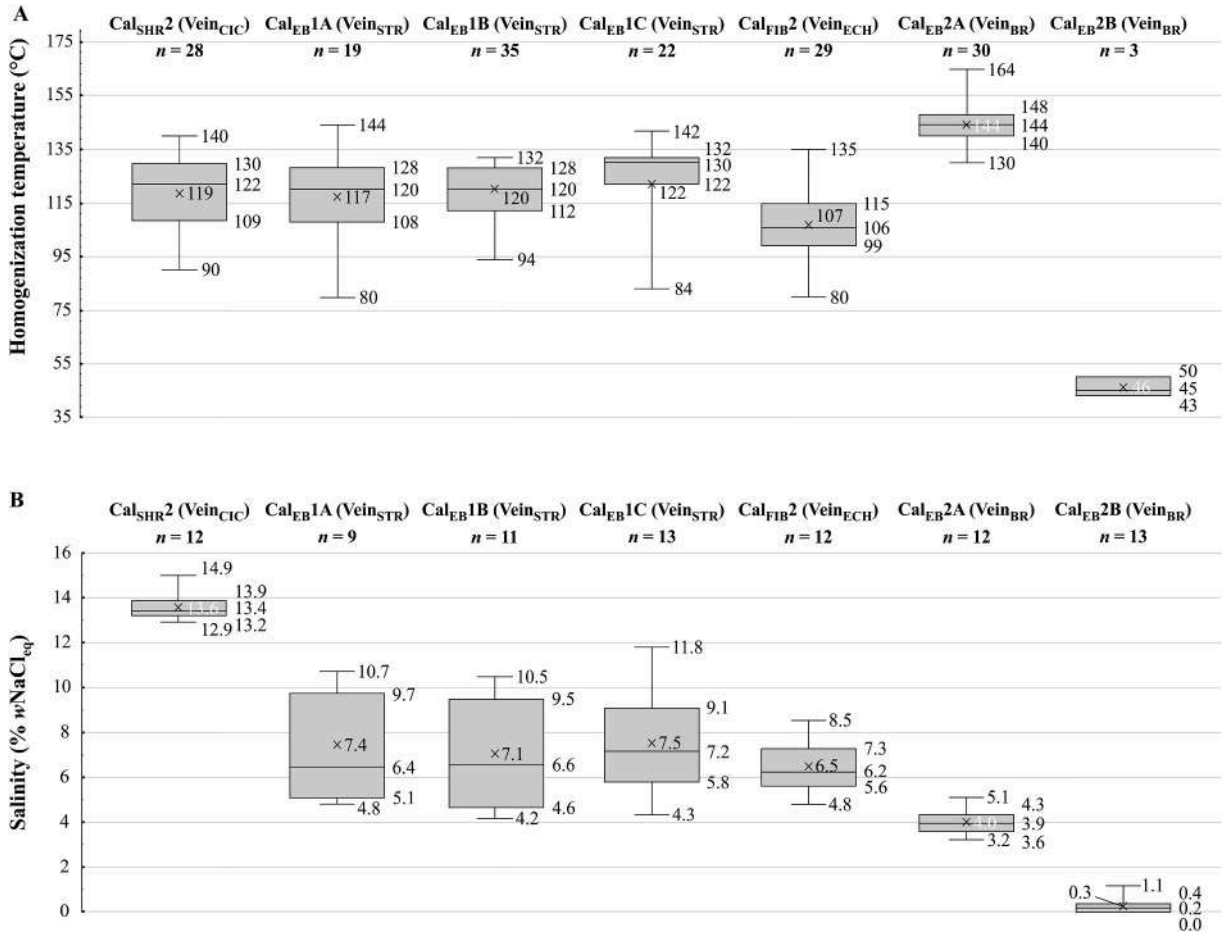

Fig. 13. Box-plot diagrams of homogenization temperatures (A) and salinity (B) measured in the $Cal_{SHR}2$, $Cal_{EB}1A$, $Cal_{EB}1B$, $Cal_{EB}1C$, $Cal_{FIB}2$, $Cal_{EB}2A$ and $Cal_{EB}2B$ mineral phases of the $Vein_{CIC}$, $Vein_{STR}$, $Vein_{ECH}$ and $Vein_{BR}$ generations. The box represents the first and third quartiles of the data on the diagrams, the X and the band inside the box indicate the mean and median values.

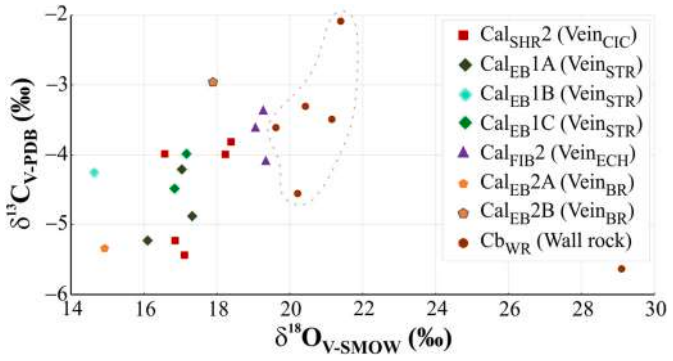

Fig. 14. Carbon and oxygen isotopic compositions of vein-filling calcite and wall rock carbonates from the BAF–2 well. The values of Cb_{WR} are marked out with a grey dashed line.

Cal_{EB}2A phase ($Vein_{BR}$) indicate a parent fluid of higher temperature (typical values are from 140 to 148 °C, Figs. 12, 13 and 17); while most of the FIs in the Cal_{EB}2B are single-phase at room temperature representing trapping temperatures below 50 °C (nucleation metastability; Goldstein and Reynolds, 1994). Within the Cal_{EB}2B phase, the T_h of three two-phase FIs could be measured (43–50 °C), which, together with T_m (Ice) values measured after the artificial stretching of the FIs, also supports the low formation temperature of the Cal_{EB}2B.

Although the T_h values of $Vein_{CIC}$ and $Vein_{STR}$ veins are in the same range, the T_m (Ice) values (Fig. 16) indicate higher salinity level (between 13.3 and 13.7% $wNaCl_{eq}$) in the $Vein_{CIC}$, than it is usual in the $Vein_{STR}$ (4.6–9.7% $wNaCl_{eq}$). The $Vein_{ECH}$ has a salinity between 5.6 and 7.3% $wNaCl_{eq}$. Within the $Vein_{BR}$ samples, the FIs of the Cal_{EB}2A phase indicate a parent fluid of 3.5–4.3% $wNaCl_{eq}$ salinity, while the FIs of Cal_{EB}2B suggest low salinities (0.0–0.4% $wNaCl_{eq}$). In other words, based on petrographic evidence and fluid inclusion salinity data, a decreasing salinity trend can be observed from the oldest (Cal_{SHR}2, $Vein_{CIC}$) to the youngest (Cal_{EB}2B, $Vein_{BR}$) vein-forming calcite phase (Fig. 13B).

Using the fractionation equation of O'Neil et al. (1969), the equilibrium isotope fractionation factor (α) for the distribution of ^{18}O between the carbonate and its parent fluid can be calculated for a given temperature. Accepting the measured T_h values as crystallisation temperatures and knowing the $\delta^{18}O$ compositions of the mineral phases, the fractionation factors reveal the $\delta^{18}O$ compositions of the parent fluids (Fig. 17). The calculated $\delta^{18}O_{water}$ (V-SMOW) values generally underestimate the original water composition, since the used T_h values without pressure correction represent the minimum trapping temperatures (Goldstein and Reynolds, 1994; Diamond, 2003).

The calculated $\delta^{18}O$ compositions of most parent fluids fall between a close range from −0.72 to 4.67‰ (V-SMOW), which overlap significantly with the characteristic values of basinal brines (Fig. 17). Only the Cal_{EB}2B phase matches the estimated values of meteoric waters suggesting its origin. The chemical composition of "basinal brines" or "formation waters" in the case of a fossil playa sequence might result from complex diagenetic processes. The initial fluid composition of the

Table 2
Carbon and oxygen isotopic compositions of the studied samples.

Sample ID	Total Measured Depth (m)	Sample type	Measured mineral phase	$\delta^{13}C$ (‰, V-PDB)	$\delta^{18}O$ (‰, V-SMOW)
BAF–2_074	74	Wall rock	Cb_{WR}	−2.08	21.39
BAF–2_251/1	251	$Vein_{STR}$	$Cal_{EB}1A$	−4.20	17.03
BAF–2_251/2	251	$Vein_{CIC}$	$Cal_{SHR}2$	−3.98	16.57
BAF–2_283/1	283	$Vein_{ECH}$	$Cal_{FIB}2$	−4.08	19.34
BAF–2_283/2	283	Wall rock	Cb_{WR}	−3.49	21.14
BAF–2_356	356	$Vein_{STR}$	$Cal_{EB}1C$	−3.98	17.16
BAF–2_500	500	$Vein_{ECH}$	$Cal_{FIB}2$	−3.36	19.26
BAF–2_548	548	$Vein_{BR}$	$Cal_{EB}2B$	−2.95	17.89
BAF–2_608/1	608	$Vein_{CIC}$	$Cal_{SHR}2$	−3.81	18.39
BAF–2_608/2	608	$Vein_{CIC}$	$Cal_{SHR}2$	−3.99	18.22
BAF–2_608/3	608	Wall rock	Cb_{WR}	−3.30	20.42
BAF–2_657	657	$Vein_{ECH}$	$Cal_{FIB}2$	−3.61	19.05
BAF–2_720/1	720	$Vein_{STR}$	$Cal_{EB}1C$	−4.48	16.83
BAF–2_720/2	720	$Vein_{STR}$	$Cal_{EB}1A$	−5.23	16.10
BAF–2_720/3	720	$Vein_{STR}$	$Cal_{EB}1B$	−4.25	14.63
BAF–2_720/4	720	Wall rock	Cb_{WR}	−3.61	19.60
BAF–2_760/1	760	$Vein_{CIC}$	$Cal_{SHR}2$	−5.23	16.85
BAF–2_760/2	760	$Vein_{CIC}$	$Cal_{SHR}2$	−5.43	17.11
BAF–2_760/3	760	Wall rock	Cb_{WR}	−4.55	20.20
BAF–2_767/1	767	$Vein_{BR}$	$Cal_{EB}2A$	−5.33	14.92
BAF–2_767/2	767	Wall rock	Cb_{WR}	−5.62	29.09
BAF–2_831	831	$Vein_{STR}$	$Cal_{EB}1A$	−4.87	17.31

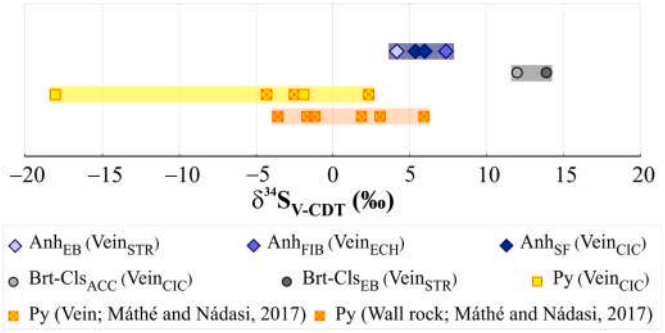

Fig. 15. Sulphur isotopic compositions of vein-filling anhydrite (Anh_{EB}; Anh_{FIB}; Anh_{SF}), barite-celestine ($Brt\text{-}Cls_{ACC}$; $Brt\text{-}Cls_{EB}$), and pyrite (Py) supplemented with $\delta^{34}S$ values of wall rock and vein-filling pyrite from the BAF–2 well observed by Máthé and Nádasi (2017).

sediments in such low permeability formations is crucial. According to Rosen (1994), the playa brine can be derived from two primary sources: 1) directly from meteoric precipitation, 2) from groundwater of meteoric-, connate seawater-, or deep basinal hydrothermal origin. In the case of the BCF, seawater origin can be excluded, due to long-lasting continental sedimentation during the Paleozoic evolution of the studied region. Thus, the most probable source of the initial pore fluids of the BCF is meteoric; however, the presence of upward percolating hydrothermal fluids during sedimentation cannot be excluded either. During the sedimentation and shallow diagenesis of playa sediments, the evaporation is the most significant process, that leads to ^{18}O enrichment and increasing salinity in the pore fluids (Rosen, 1994; Liutkus and Wright, 2007). Due to the mineralogical composition and low permeability of the BCF, a relatively closed hydrological system can be assumed during and after the main compaction phase of the formation. In this closed hydrological system water-rock interactions, isotopic exchange with ^{18}O-rich sedimentary carbonates (Hoefs, 2009), and clay mineral alterations are the main processes that might change the composition of the formation waters. Since the illite is one of the main mineralogical compounds of the BCF (Árkai et al., 2000; Máthé, 2015), water release during smectite-to-illite transformation might have played an essential role in the chemical composition of the pore waters. This transition generally occurred at elevated temperatures (120–165 °C) and resulted in increasing $\delta^{18}O$ values (up to 5–10‰ V-SMOW) and dilution of saline porewaters by freshwaters (Suchecki and Land, 1983; Fitts and Brown, 1999; Dählmann and de Lange, 2003). Thus, the basinal brines representing the parent fluids of $Cal_{SHR}2$, $Cal_{EB}1A$, $Cal_{EB}1B$, $Cal_{EB}1C$ and $Cal_{FIB}2$ vein-filling cement phases might originate from the mixture of connate playa water and clay mineral released diagenetic waters. To summarise, the source of parent fluids of the vein-forming calcite phases in the $Vein_{CIC}$, $Vein_{STR}$ and $Vein_{ECH}$ can be explained by the mixture of locally derived formation waters and diagenetic reactions (closed geochemical system). In contrast, the youngest, $Cal_{EB}2B$ phase of the $Vein_{BR}$ was probably precipitated from a low-temperature (<50 °C) meteoric fluid representing an open geochemical system, where meteoric water recharge was potentially related to tectonic uplift (Gál et al., 2020).

The narrow range of $\delta^{34}S$ values of all anhydrite phases suggests their identical origin, valid for the measured $Brt\text{-}Cls_{ACC}$ and $Brt\text{-}Cls_{EB}$ phases. Based on the $\delta^{34}S$ values of vein-forming sulphates Hertelendi (1996) suggested, that barite and anhydrite phases from different locations (tunnel α–1, boreholes BAT–4 and BAT–5) were precipitated directly in the lake environment. However, the observed euhedral sulphides or acicular barite-celestine morphologies and the mineral assemblages in the BAF–2 well (e.g. Ab, Cal, Chl, Py–Ccp, Gn; Figs. 5, 7 and 9) contradict this suggestion. Based on mineral composition and FI data of anhydrite-bearing veins, Máthé (1999) concluded, that low-temperature hydrothermal solutions dissolved the sulphate minerals formed in the lake environment, and precipitated later in fractures and veins. Our observations from the BAF–2 well on the sulphate morphologies and $\delta^{34}S$ values analogous to Hertelendi (1996) result support Máthé (1999) assumption.

The scattered $\delta^{34}S$ values of Py-Ccp crystals are more difficult to interpret because they can be related to different sulphide formation models, such as bacterial, thermochemical, or hydrothermal, as proposed by Máthé and Nádasi (2017). To determine what type of mechanism was characteristic of the BCF, the details of the possible processes are summarised.

(1) Bacterial sulphate reduction (BSR). In anoxic conditions, dissolved sulphates (SO_4^{2-}) are reduced to hydrogen sulphide (H_2S) by bacteria while oxidising organic material (CH_2O, idealised formula) to CO_2, which reacts with water to form carbonic acid (H_2CO_3) dissociating later to bicarbonate (HCO_3^-) and hydrogen ions (H^+) (Berner, 1984; da Costa et al., 2017):

$$2CH_2O + SO_4^{2-} \rightarrow H_2S + 2HCO_3^- \quad (1)$$

Table 3
Sulphur isotopic compositions of the studied samples supplemented with $\delta^{34}S$ values of wall rock and vein-filling pyrite from the BAF–2 well observed by Máthé and Nádasi (2017). n.d.–no data.

Sample ID	Total Measured Depth (m)	Sample type	Measured mineral phase	$\delta^{34}S$ (‰, V-CDT)	References
G–43492	150	Wall rock	Py	−3.60	Máthé and Nádasi (2017)
BAF–2_622/1	622	$Vein_{CIC}$	Brt-Cls_{ACC}	12.00	This study
BAF–2_622/2	622	$Vein_{CIC}$	Py	−18.01	This study
BAF–2_644	644	$Vein_{STR}$	Anh_{EB}	4.14	This study
BAF–2_657	657	$Vein_{ECH}$	Anh_{FIB}	7.35	This study
G–43590	709	Wall rock	Py	−1.20	Máthé and Nádasi (2017)
G–43592	717	Wall rock	Py	1.90	Máthé and Nádasi (2017)
BAF–2_720	720	$Vein_{STR}$	Brt-Cls_{EB}	13.88	This study
G–43596	727	Wall rock	Py	−1.70	Máthé and Nádasi (2017)
G–43596	727	Vein (n. d.)	Py	2.40	Máthé and Nádasi (2017)
BAF–2_760/1	760	$Vein_{CIC}$	Anh_{SF}	5.35	This study
G–43602	760	Vein (n. d.)	Py	−4.30	Máthé and Nádasi (2017)
G–43605	830	Wall rock	Py	3.10	Máthé and Nádasi (2017)
BAF–2_831/1	831	$Vein_{CIC}$	Anh_{SF}	5.90	This study
BAF–2_831/2	831	$Vein_{CIC}$	Py	−1.86	This study
G–43608	841	Vein (n. d.)	Py	−2.50	Máthé and Nádasi (2017)
G–43614	884	Wall rock	Py	5.90	Máthé and Nádasi (2017)
G–43616	897	Wall rock	Py	−3.60	Máthé and Nádasi (2017)

The hydrogen sulphide reacts with solid reactive iron minerals (e.g. hematite, Fe_2O_3) to form amorphous ferrous sulphide, or metastable, disordered mackinawite (FeS) (Furukawa and Barnes, 1995; Wilkin and Barnes, 1996; Csákberényi-Malasics et al., 2012). Later, during a series of reactions [H_2S (Rickard, 1997; Rickard and Luther, 1997) or polysulphide (S_n^{2-}) pathways (Rickard, 1975; Luther, 1991)] pyrite (FeS_2) forms (Butler et al., 2004; Rickard and Luther, 2007). The simplified, net reactions without indicating sub-processes are:

$$FeS_{(s)} + H_2S_{(aq)} \rightarrow FeS_{2(s)} + H_{2(g)} \quad (2)$$

$$FeS_{(s)} + S_n^{2-}{}_{(aq)} \rightarrow FeS_{2(s)} + S_{n-1}^{2-}{}_{(aq)} \quad (3)$$

In the presence of alkaline earth metals, in addition to sulphides, carbonates such as calcite and dolomite may form. These processes work ideally between 0 and 80 °C (Machel et al., 1995; Machel, 2001), but may operate up to a maximal temperature of 120 °C (Goldstein and Aizenshtat, 1994) depending on the species of sulphate-reducing microorganisms. These reducing bacteria produce sulphides depleted in ^{34}S by 15–65‰ relative to the parent sulphate (Machel et al., 1995).

(2) Thermochemical sulphate reduction (TSR). The organic material reduces sulphate by abiogenic, chemically controlled reactions (Goldstein and Aizenshtat, 1994) yielding dissolved H_2S commonly between temperatures of 100–200 °C (Machel, 2001). Later, carbonate and, as shown by reaction (3) and (4), pyrite can form. The primary sources of dissolved sulphate can be seawater, evaporative brines, and dissolving calcium sulphates such as gypsum ($CaSO_4 \bullet 2H_2O$) and anhydrite ($CaSO_4$). If a higher amount of organic material and sulphates are available, a higher amount of sulphides form. Sulphides produced by TSR are depleted in ^{34}S by 10–20‰ relative to the parent sulphate (Machel et al., 1995).

(3) Hydrothermal activity. In deposits of hydrothermal origin, metallic minerals precipitate from high-temperature (~50–500 °C) fluids (Pirajno, 2009). The source of hydrothermal solution can be seawater, meteoric (including rain-, lake-, river-, and groundwaters), connate, metamorphic, juvenile or magmatic (Pirajno, 2009). In most cases, the hydrothermal solutions are mixtures of fluids with different origin in variable amounts. The fluids can be heated by various means, such as magmatic activity, geothermal gradient, radiogenic decay or metamorphism (Pirajno, 2009). These heated fluids can leach, transport and reprecipitate minerals in response to physico-chemical changes. In magmatic-hydrothermal ore deposits, where magmatic water is a significant, but not exclusive fluid component (Taylor, 1974), the $\delta^{34}S$-values of sulphides are dominantly between −3 and 1‰, and of sulphates between 8 and 15‰, respectively (Hoefs, 2009). In other hydrothermal ore deposits, the $\delta^{34}S$-values are less consistent because of less stable controlling factors, such as temperature, the isotopic composition of dissolved S, and SO_4^{2-} – H_2S ratio in the fluid, which depends on pH and f_{O2} (Pirajno, 2009).

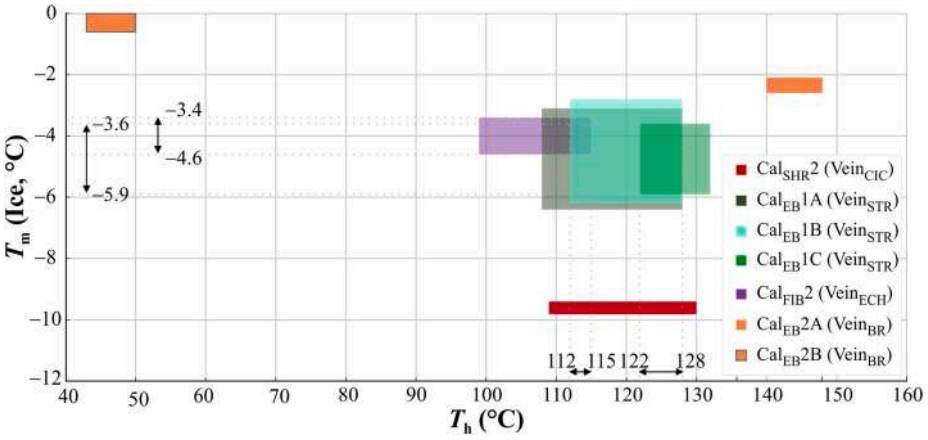

Fig. 16. T_m (Ice) vs T_h diagram of typical values measured in vein-forming calcite phases.

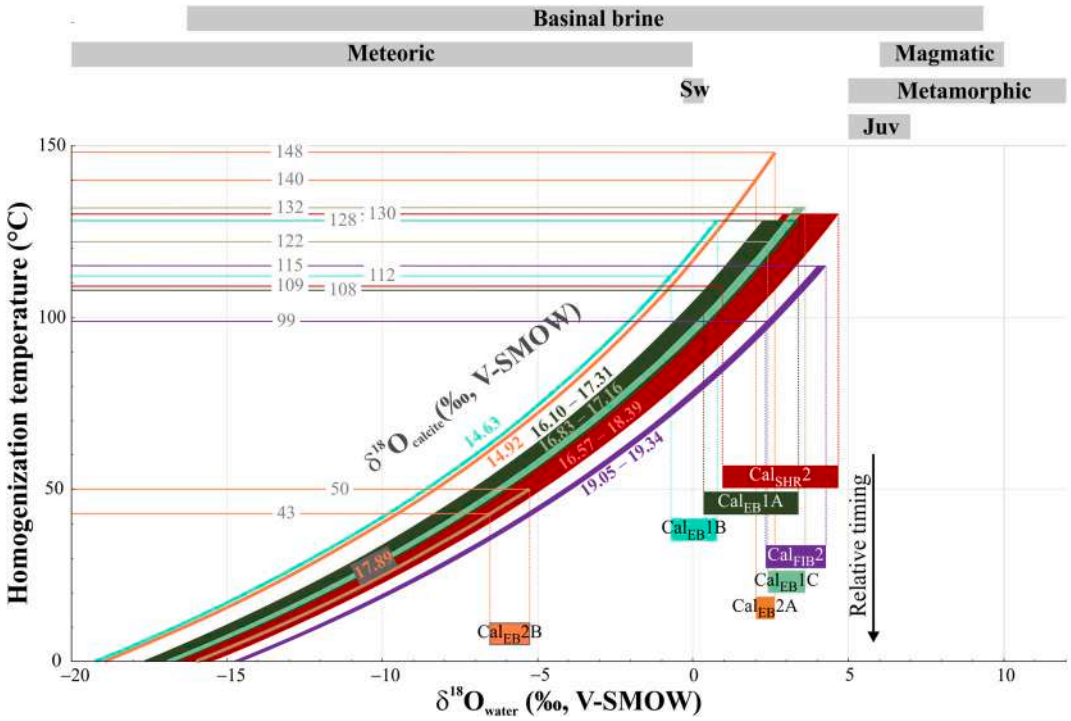

Fig. 17. Homogenization temperature–$\delta^{18}O_{water}$ (‰, V-SMOW) diagram of the vein-forming calcite phases. The curved lines and zones represent $\delta^{18}O$ compositions of different mineral phases, while the coloured straight bands correspond to the calculated $\delta^{18}O$ compositions of parent fluids. The straight grey bands indicate the $\delta^{18}O$ of waters of various origins (Taylor, 1974; Hoefs, 2009). Juv–juvenile water; Sw–seawater.

The euhedral to subhedral Py-Ccp morphologies and positive $\delta^{34}S$ values raise the possibility of magmatic-hydrothermal mineralisation. Contrarily, the negative isotope compositions (Fig. 15, Table 3) and amorphous sulphide aggregates of fibrous crystals (Fig. 5E) advocate the possibility of BSR or TSR type sulphide formation; nevertheless, the necessary reactive organics (solid or liquid hydrocarbon residues) have not been observed in the veins. On the other hand, Berner (1984) pointed out that the H_2S, necessary for BSR or TSR type sulphide formation, can be transported from organic-rich locations. Thus, organic material oxidation and sulphate reduction are not required to occur where the iron minerals are present. In this way, H_2S-containing fluids may migrate along fractures reacting with the wall rock minerals leading to sulphide formation. One of the cation source minerals in the BCF may have been the hematite cement of the wall rock, which may have reacted with H_2S to yield sulphide phases. The leaching process is evidenced by the faded WRIs and vein walls around the observed sulphide phases (Fig. 5G). Since $\delta^{34}S$-values are not sufficient alone to distinguish between different sulphur sources (Machel et al., 1995; Hoefs, 2009), other properties need to be considered. Based on the relatively small fractionation (negative $\delta^{34}S$-values are usually between −5 and 0‰) which characterise TSR (Pirajno, 2009), on the reasonably narrow precipitation zones (Fig. 5F and G), and the lack of framboidal crystal morphologies, TSR may have been the dominant sulphide-forming process in the veins (Machel et al., 1995). Even though, the maximal ^{34}S-depletion is slightly higher (<22.15‰), between the potential parent sulphate (sample BAF–2_644) and the sulphide phases than usual (−20 to −10‰ between 100 and 200°C; Machel et al., 1995) for thermogenic sulphate reduction.

5.3. Potential vein formation processes and integration into the area's tectonic evolution

The microstructural, mineralogical and geochemical features of the observed veins from the Permian Boda Claystone Formation (BAF–2 well), in accordance with previous studies, suggest the following evolution (Fig. 18):

5.3.1. Diagenetic processes recorded by $Vein_{CIC}$ and wall rock

As proposed by many authors (Árkai et al., 2000; Varga et al., 2005; Konrád et al., 2010; Máthé and Varga, 2012; Máthé, 2015), the BCF was deposited in a playa environment under arid to semi-arid climate. Due to evaporation, the brine concentrated and evaporite minerals precipitated as hopper crystals and beds (Máthé and Varga, 2012). In deeper parts of

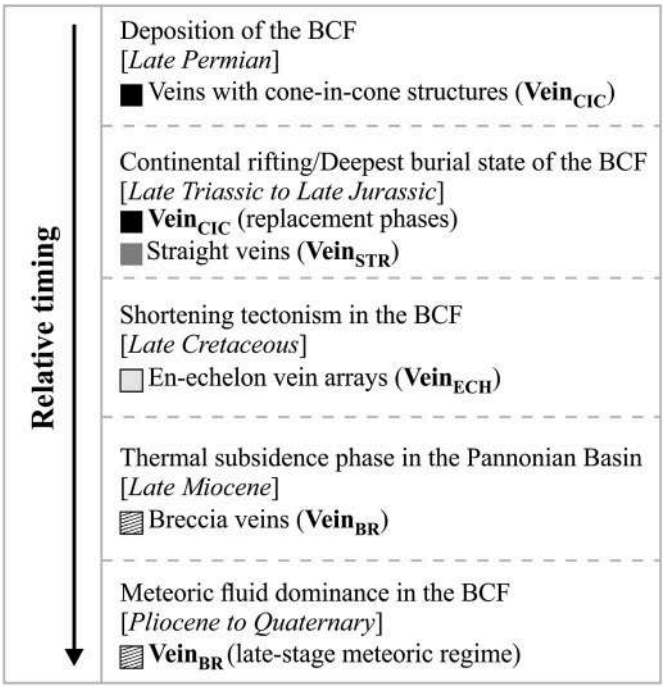

Fig. 18. Tectono-chronological evolution of the BCF recorded by veins in the BAF–2 well. In the boxes, colour codes of veins are shown, which were used coherently throughout the manuscript.

the sediment, due to upward seepage and saturation of connate waters (decreasing fluid pressure with decreasing depth) induced by growing overburden load, early diagenetic (eogenetic) displacive veins ($Vein_{CIC}$) were formed (Hrabovszki et al., 2020). At a later stage (greater burial depths and by inference, temperature) of diagenesis (burial, mesogenetic), thermodynamically stable authigenic albite ± K-feldspar (Máthé, 1999, 2015; Árkai et al., 2000; Varga et al., 2005) formed. The authigenic formation of albite needs high H_4SiO_4 activities and Na^+/H^+ ratio; therefore, the process is limited by the supply of sodium and silica (Kastner and Siever, 1979). Detrital plagioclase has a sufficient amount of sodium to yield authigenic albite, but in less volume than the original plagioclase. In the BCF, which diagenetic albite content can exceed 50 wt% in certain cases (e.g. albitolite sections), the albitisation process may have required an external sodium source (Lee and Lee, 1998). Depending on the supply of silica and alkali metals, there are several geochemical models for authigenic feldspar formation (Kastner and Siever, 1979). In isochemical models (closed system) the essential components (Na^+, Al^{3+}, Si^{4+}) are present in the sediment (e.g. marine sediment with trapped seawater, volcaniclastic sediment with trapped lake-derived water). Silica can be released by the dissolution and alteration of biogenic substances and/or volcanic glass, detrital feldspars and clay minerals. Sources of alkali metals can be trapped seawater, evaporite minerals dissolved by pore waters, diagenetic conversion of smectite to illite (Boles and Franks, 1979), replacement of detrital feldspars. In exchange reservoir (open system) models not all the essential components originate from the host rock. The transport of fluids from different reservoirs (e.g. brine from evaporite sections, magmatic-hydrothermal fluids) results in sufficient chemical composition in the pore water of the host rock for albitisation; therefore, adequate permeability is required. In the case of the BCF, no external source was needed for albitisation, since trapped brine, dissolving evaporite minerals and detrital feldspar grains were probably available. As part of the albitisation process, Ca^{2+} was added to the solution, which reacted with the dissolved HCO_3^- derived from organic material–sulphate reaction (see Equation (1)), in this way carbonate ($Cal_{SHR}1$) may have also precipitated as proposed by Varga et al. (2005). The dissolution of evaporite minerals (e.g. halite, anhydrite) supplied Na^+ for albitisation and reactive sulphate (SO_4^{2-}) for sulphide formation. The released Al^{3+} and silica from detrital feldspars (see Equation (1)) combined with Mg^{2+} and Fe^{2+} from the dissolution of detrital mafic minerals (Varga et al., 2005) may have led to clay mineral (chlorite) formation (Burley and Worden, 2003). The authigenic feldspar and carbonate phases precipitated in the groundmass as pervasive cement (Máthé, 2015), as replacing hopper halite crystals (Máthé and Varga, 2012) and the original fibrous vein-filling of $Vein_{CIC}$ (Hrabovszki et al., 2020).

To summarise, there are two potential scenarios for the formation of the above-mentioned Ab ± Kfs, $Cal_{SHR}1$, Chl and Py-Ccp mineral phases observed in the $Vein_{CIC}$ (and within the wall rock): (1) Diagenetic albitisation combined with thermochemical sulphate reduction, chlorite and calcite formation due to isochemical hydrothermal processes. In this case, the mineralisation resulted from heated connate brines, which dissolved and reprecipitated minerals in thermodynamically stable forms. (2) Diagenetic albitisation followed by hydrothermal mineralisation induced by magmatic activity. In this case, after diagenetic albite formation, magmatic-hydrothermal solutions migrated through the pores and fractures of the rock body, mixed with the formation waters, and leached, transported, then deposited calcite, chlorite and sulphide minerals.

In our view, the first option is more reasonable based on the followings: (a) based on petrography, the Ab-Kfs-Py-Ccp-Gn-$Cal_{SHR}1$-Chl minerals form a syngenetic assemblage (Fig. 5). (b) The $\delta^{34}S$ values of sulphides and sulphates cover a wider range than typical in magmatic deposits (Hoefs, 2009). (c) The amorphous, fibrous sulphide phase (FeS_{FIB}, Fig. 5E) can be interpreted as a precursor of pyrite formation (Berner, 1984; Furukawa and Barnes, 1995). (d) The sulphide- and TOC content of the formation is closely related (Máthé and Nádasi, 2017), see Chapter 5.2.

Considering, that the albitisation was potentially diagenetic (Árkai et al., 2000; Varga et al., 2005), the associated mineralisation, such as calcite, sulphide and chlorite formation is also a syn-diagenetic process. As discussed above, the albitisation and sulphide formation require increased temperature. Considering the tectonic evolution of the study area, it cannot be ruled out that the heating event is related to the Penninian rifting, which resulted in the separation of the Tisza Mega-unit from the European plate. Simultaneously with the rifting, the BCF might have reached deep diagenetic to low anchizone conditions in the Late Triassic to Jurassic period based on IC, ChC, vitrinite reflectance values and K-white mica K–Ar ages (Árkai et al., 2000).

5.3.2. *Dissolution, reprecipitation and extensional tectonics recorded by $Vein_{CIC}$ and $Vein_{STR}$*

After the formation of Ab-Kfs-Py-Ccp-Gn-$Cal_{SHR}1$-Chl phases, the remaining evaporite minerals dissolved from the $Vein_{CIC}$ and the pores within the veins were filled partly, from intraformational, advectively migrating fluids, by $Cal_{FIB}1$-$Cal_{SHR}2$-Brt-Cls_{ACC}-Py-Ccp-Gn assemblage. The initial presence of evaporite minerals within the $Vein_{CIC}$ was suggested by Hrabovszki et al. (2020) and is evidenced by the relatively high (13.3–13.7% $wNaCl_{eq}$) salinity, which may have resulted from the dissolution of evaporite minerals. Based on petrography and isotopic data, the second generation of sulphides appearing in the pores of $Cal_{FIB}1$-$Cal_{SHR}2$ phases of $Vein_{CIC}$ may also have been formed by TSR, as discussed in Chapter 5.3.1. The Brt-Cls_{ACC} may have originated as suggested by Máthé (1999): heated formation water dissolved this mineral, initially formed in the playa environment, and reprecipitated it in veins. The subsidence during an advanced stage of the Penninian rifting may have been responsible for the elevated temperature.

Comparing T_h values and stable isotope ratios measured in $Cal_{SHR}2$-Brt-Cls_{ACC} ($Vein_{CIC}$) and $Cal_{EB}1$A-B-C-Brt-Cls_{EB} ($Vein_{STR}$) phases reveals that their parent fluids are of similar origin. Nevertheless, the lower salinity (4.6–9.7% $wNaCl_{eq}$) of $Vein_{STR}$ phases suggests, that the connate brine was diluted by freshwater from clay mineral transitions (details in Chapter 5.2). Based on the nature of the $Vein_{STR}$, i.e. hybrid fracturing, the evolution of $Vein_{STR}$ is related to extensional tectonics, which could have been associated with a later, tectonically active period of the Penninian rifting. In the first stage, heated formation waters migrated advectively in the pores of the rock body, and precipitated $Cal_{EB}1$A and Brt-Cls_{EB} phases in fractures forming syntaxial veins. In the second stage, the veins re-opened and filled with the $Cal_{EB}1$B phase.

5.3.3. *Compressional tectonics and anhydrite precipitation recorded by $Vein_{ECH}$, $Vein_{STR}$ and $Vein_{CIC}$*

The $Vein_{ECH}$ may have developed in a compressional stress field that can potentially be related to the Late Cretaceous stage of the Alpine orogeny. During this event, folds with NE–SW axis orientation were formed in the Mecsek Mountains (Benkovics et al., 1997). Based on the constant dip of the shear zones throughout the BAF–2 well, Tóth et al. (2020) concluded, that the formation of the $Vein_{ECH}$ sets took place more or less simultaneously with or after the folding. The structural evolution related to this compressional stress field has led to the formation of veins with different kinematics and composition. The $\delta^{13}C$ and $\delta^{18}O$ composition of $Cal_{FIB}2$ are close to the values measured in the wall rock, which indicates rock-dominated fluid-rock interaction. The origin of the parent fluid may be similar to that of the $Cal_{EB}1$A-B-C phases, namely, high temperature (99–115 °C) formation water (basinal brine) interacted with the host rock through different chemical reactions. The Brt-Cls_{FIB} can be interpreted as the dissolved and reprecipitated form of the playa-derived minerals. After the shear zone development, anhydrite precipitated in the formation. Parts of $Cal_{FIB}2$, Brt-Cls_{FIB} and $Cal_{EB}1$B phases were replaced by Anh_{FIB} and Anh_{EB} in the $Vein_{ECH}$ and $Vein_{STR}$ (Figs. 9 and 7A, C). The remaining pores of $Vein_{CIC}$ were partially, or in cases completely, filled by Anh_{SF} (Fig. 5D, F, H).

5.3.4. Mobile hydrofracture, influence of meteoric fluids recorded by $Vein_{STR}$ and $Vein_{BR}$

After the anhydrite precipitation, $Cal_{EB}1C$ with Qtz_{FG} sealed the re-opened $Vein_{STR}$. This calcite-quartz assemblage may have also precipitated as fibrous crystals in the wall rock ($Cal_{FIB}3$ and Qtz_{FIB} in $Vein_{BR}$). The parent fluid could be the formation water, which interacted with the sedimentary minerals. These initial fibrous crystals of the $Vein_{BR}$ may have served as weakness planes during later vein evolution. The high amount of angular-shaped WRIs, which can perfectly be matched together (in-situ fragmentation textures; Fig. 11) suggests that the vein development is related to fluid-associated, hydraulic brecciation (Jébrak, 1997). The increase in fluid pressure required for hydraulic brecciation can be derived from several factors, such as increased heat, compaction, hydrocarbon generation, decrease in fault permeability or tectonic uplift (Jébrak, 1997; Beaumont and Fiedler, 1999; Cobbold and Rodrigues, 2007). In case of BCF, tectonic uplift during the inversion of the Pannonian Basin could be a reasonable cause of fluid pressure increase; however, Konrád and Sebe (2010) pointed out that no sign of post-Miocene tectonic activity can be found in the Western Mecsek Mts. Another explanation could be that the increased heat elevates the pressure in contained pore fluid. As a result, fractures can form along planes of weakness associated with brecciation. These fractures could propagate with the pore fluid (mobile hydrofractures) as proposed by Bons (2001), which can cement the fragments of the wall rock by the precipitation of dissolved matter. In $Vein_{BR}$, the relatively high T_h values (Figs. 13A and 17) observed in $Cal_{EB}2A$ supports this concept. Accordingly, the elevated temperature and the brecciation could be related to the post-rift phase of the Pannonian Basin. Later, low-temperature (T_h = 43–50 °C) meteoric waters migrated in the pores of $Vein_{BR}$ and precipitated the texturally and geochemically different $Cal_{EB}2B$ phase indicating the Neogene subaerial exposure of the BCF.

5.4. Relevance of the study for the nuclear waste storage development

The utilization of natural resources, the avoidance of harmful environmental effects, and thus the long-term protection of our environment are key in the management of radioactive waste. It is critical to find a long-term stable geological environment for disposal of high-level radioactive waste. Furthermore, it is important to classify potential sites and find optimal locations for repositories within geological formations, since some processes may result in the release of radionuclides located in the repository. These processes may include the gradual degradation of engineered barriers or an unexpected decrease in the isolation capacity of the geological barrier through tectonic processes. In this research, we investigated the potential geological formation of the waste repository in Hungary, the Boda Claystone Formation, to gain information about tectonic effects and fluid migration events that characterise the rock body's more than 250-million-year-old history. The mineral veins appearing in the BCF were formed during four major events. The earliest event was related to atectonic, diagenetic processes ($Vein_{CIC}$). This was followed by an extensive tectonic phase in which minerals were precipitated from advectively migrating fluids, cementing the fractures in several phases ($Vein_{STR}$). In the next, compressional tectonic phase, shear zones consisting of sigmoidal tension gashes ($Vein_{ECH}$) were formed. However, these zones did not function as fluid migration pathways, and the constituents of the minerals cementing the tension gashes may have reached their position during local, diffusional processes. The parent fluids of the minerals that form the above-mentioned three vein generations presumably originated from within the BCF, revealing the outstanding fluid-barrier properties of the rock body. During the last structural event, hydraulic breccias ($Vein_{BR}$) were formed. In their pores, a mineral phase was precipitated, suggesting the advective flow of low salinity, external fluids. Gál et al. (2020) pointed out that the latest structural-diagenetic features can potentially record the fluid salinity conditions that are also representative for the present day. This consideration in the BCF is supported by the low salinity (<0.5% $wNaCl_{eq}$) of water samples collected from different depth intervals (310–336 m; 484–509 m; 860–886 m) of the BAF–2 well. It is worth noting that the upper two water samples are of sodium bicarbonate type, while the lower sample shows a significantly different, sodium sulphate character (Sámson, 2015). Although breccias are not common in the BCF, their open pores may pose a safety risk during the long-term operation of the facility, meaning that assessing their frequency, spatial location, connectivity, and fluid conductivity deserves special consideration in selecting the appropriate site.

6. Conclusions

Based on vein petrography and geochemistry, the development of veins in the BCF started during the early diagenetic evolution of the formation. The original filling of the earliest vein generation ($Vein_{CIC}$, which is an early, displacive vein; Hrabovszki et al., 2017) was replaced by albite ± K-feldspar, chlorite, sulphides, and carbonates in the presence of connate brines. The origin of these mineral phases could potentially be related to diagenetic albitisation and thermochemical sulphate reduction induced by increased temperature achieved during the Penninian rifting in the Late Triassic to Jurassic period. The vein-filling sulphides could be interpreted as sedimentary-hosted hydrothermal mineral deposits. In a later stage of structural evolution, crack-seal veins were formed via mineral precipitation from 110 to 130 °C formation waters, which, based on $\delta^{18}O$ values and FI data, were connate brines diluted by freshwater from clay mineral alterations. In this way, carbonates and sulphates formed in at least three major, and several minor, cracking and sealing events from intraformational, advectively migrating fluids ($Vein_{STR}$). These fluids may have also migrated in the pores of the pre-existing veins precipitating the above-mentioned minerals. During the next deformation phase, shear zones were formed by the antitaxial growth of en-echelon veins ($Vein_{ECH}$). The $\delta^{18}O$ and T_h values of fibrous vein-filling crystals indicate a strong interaction between the parent fluid (formation water) and the wall rock, suggesting that the primary material transport mechanism was diffusion. At this stage, some of the pre-existing veins were also re-opened and cemented. A next, formation-wide event was the anhydrite precipitation. Based on vein textures and $\delta^{34}S$ values, potentially the early evaporative minerals were transported from the wall rock and reprecipitated in all existing veins. During the last tectonically active phase, fractures propagated along former weakness planes with 140–150 °C fluids creating hydraulic breccias ($Vein_{BR}$). More recently, low-temperature (43–50 °C) meteoric fluids migrated in the pores of these breccias precipitating the youngest vein-filling calcite phase.

To summarise, the origin of the fracture-filling calcite in most cement phases can be explained by precipitation from locally derived pore fluids formed by the mixture of saline connate water of playa sediments with components resulting from diagenetic reactions (e.g. clay mineral transitions). In the youngest vein-filling calcite phase, the parent fluid was meteoric in origin and probably represents downward fluid migration through the breccia veins. In other words, the $Vein_{CIC}$, $Vein_{STR}$ and $Vein_{ECH}$ fractures were cemented by minerals precipitated from intraformational fluids. In contrast, the mineral filling of the youngest breccia ($Vein_{BR}$) generation indicates the influence of meteoric fluids.

In this study we have demonstrated that petrographic observation coupled with geochemical analysis of veins provides an excellent opportunity to explore the many tectonic and paleofluid migration phases of the BCF and their characteristics that would have remained hidden without the combined application of these methods.

Author statement

Ervin Hrabovszki: Conceptualization, Investigation, Writing - Original Draft.
Emese Tóth: Writing - Review & Editing.
Tivadar M. Tóth: Writing - Review & Editing.
István Garaguly: Writing - Review & Editing.
István Futó: Investigation.
Zoltán Máthé: Resources, Writing - Review & Editing.
Félix Schubert: Supervision, Writing - Review & Editing.

Declaration of competing interest

The authors declare that they have no known competing financial interests or personal relationships that could have appeared to influence the work reported in this paper.

Acknowledgements

We thank János Nádasi for the helpful suggestions. László Palcsu is thanked for his assistance during stable isotope ratio measurements. Zsolt Benkó and András Fall are thanked for their comments that greatly improved the manuscript. We thank the Public Limited Company for Radioactive Waste Management (RHK Kft.) for the permission to publish the present results and the Mecsekérc Ltd. for providing the BAF–2 core samples. This work was supported by the University of Szeged Open Access Fund [grant number 5152].

References

Árkai, P., Balogh, K., Demény, A., Fórizs, I., Nagy, G., Máthé, Z., 2000. Composition, diagenetic and post-diagenetic alterations of a possible radioactive waste repository site: the Boda Albitic Claystone Formation, southern Hungary. Acta Geol. Hung. 43, 351–378.

Barabás-Stuhl, Á., 1981. A geological study of the microcycles forming the Kővágószőlős Sandstone Formation. Bulletin of the Hungarian Geological Society 111, 26–42 (in Hungarian with English abstract).

Beaumont, E.A., Fiedler, F., 1999. Formation fluid pressure and its application. In: Beaumont, E.A., Foster, N.H. (Eds.), Exploring for Oil and Gas Traps. American Association of Petroleum Geologists. https://doi.org/10.1306/TrHbk624C5.

Benkovics, L., Mansy, J.-L., Csontos, L., Bergerat, F., 1997. Folding in the Abaliget road cut (Mecsek mts). Acta Geol. Hung. 40, 425–440.

Bergerat, F., Csontos, L., 1988. Brittle tectonics and paleo-stress field in the Mecsek and Villány Mts (Hungary): correlation with the opening mechanism of the Pannonian Basin. Acta Geol. Hung. 31, 81–100.

Berner, R.A., 1984. Sedimentary pyrite formation: an update. Geochem. Cosmochim. Acta 48, 605–615. https://doi.org/10.1016/0016-7037(84)90089-9.

Bodnar, R.J., 1993. Revised equation and table for determining the freezing point depression of H_2O-NaCl solutions. Geochem. Cosmochim. Acta 57, 683–684. https://doi.org/10.1016/0016-7037(93)90378-A.

Boles, J.R., Franks, S.G., 1979. Clay diagenesis in Wilcox Sandstones of Southwest Texas: implications of smectite diagenesis on sandstone cementation. SEPM J. Sediment. Res. 49, 55–70. https://doi.org/10.1306/212f76bc-2b24-11d7-8648000102c1865d.

Boles, J.R., 1982. Active albitisation of plagioclase, Gulf Coast Tertiary. Am. J. Sci. 282, 165–180. https://doi.org/10.2475/ajs.282.2.165.

Bons, P.D., Elburg, M.A., Gomez-Rivas, E., 2012. A review of the formation of tectonic veins and their microstructures. J. Struct. Geol. 43, 33–62. https://doi.org/10.1016/j.jsg.2012.07.005.

Bons, P.D., 2000. The formation of veins and their microstructures. J. Virtual Explor. https://doi.org/10.3809/jvirtex.2000.00007, 02.

Bons, P.D., 2001. The formation of large quartz veins by rapid ascent of fluids in mobile hydrofractures. Tectonophysics 336, 1–17. https://doi.org/10.1016/s0040-1951(01)00090-7.

Burley, S.D., Worden, R.H. (Eds.), 2003. Sandstone Diagenesis: Recent and Ancient. Blackwell Publishing, Oxford. https://doi.org/10.1002/9781444304459.

Butler, I.B., Böttcher, M.E., Rickard, D., Oldroyd, A., 2004. Sulfur isotope partitioning during experimental formation of pyrite via the polysulfide and hydrogen sulfide pathways: implications for the interpretation of sedimentary and hydrothermal pyrite isotope records. Earth Planet Sci. Lett. 228, 495–509. https://doi.org/10.1016/j.epsl.2004.10.005.

Cobbold, P.R., Rodrigues, N., 2007. Seepage forces, important factors in the formation of horizontal hydraulic fractures and bedding-parallel fibrous veins ('beef' and 'cone-in-cone'). Geofluids 7, 313–322. https://doi.org/10.1111/j.1468-8123.2007.00183.x.

Cobbold, P.R., Zanella, A., Rodrigues, N., Løseth, H., 2013. Bedding-parallel fibrous veins (beef and cone-in-cone): worldwide occurrence and possible significance in terms of fluid overpressure, hydrocarbon generation and mineralization. Mar. Petrol. Geol. 43, 1–20. https://doi.org/10.1016/j.marpetgeo.2013.01.010.

Csákberényi-Malasics, D., Rodriguez-Blanco, J.D., Kis, V.K., Rečnik, A., Benning, L.G., Pósfai, M., 2012. Structural properties and transformations of precipitated FeS. Chem. Geol. 294–295, 249–258. https://doi.org/10.1016/j.chemgeo.2011.12.009.

Csontos, L., Bergerat, F., 1992. Reevaluation of the Neogene brittle tectonics of the Mecsek-Villány area (SW Hungary). Annales Universitatis Scientiarum Budapestinensis de Rolando eötvös Nominatae. Sectio geologica 29, 3–12.

Csontos, L., Vörös, A., 2004. Mesozoic plate tectonic reconstruction of the Carpathian region. Palaeogeogr. Palaeoclimatol. Palaeoecol. 210, 1–56. https://doi.org/10.1016/j.palaeo.2004.02.033.

Csontos, L., Benkovics, L., Bergerat, F., Mansy, J.-L., Wórum, G., 2002. Tertiary deformation history from seismic section study and fault analysis in a former European Tethyan margin (the Mecsek–Villány area, SW Hungary). Tectonophysics 357, 81–102. https://doi.org/10.1016/s0040-1951(02)00363-3.

da Costa, G., Hofmann, A., Agangi, A., 2017. Provenance of detrital pyrite in Archean sedimentary rocks. In: Mazumder, R. (Ed.), Sediment Provenance. Elsevier. https://doi.org/10.1016/b978-0-12-803386-9.00018-6.

Dählmann, A., de Lange, G.J., 2003. Fluid–sediment interactions at Eastern Mediterranean mud volcanoes: a stable isotope study from ODP Leg 160. Earth Planet Sci. Lett. 212, 377–391. https://doi.org/10.1016/s0012-821x(03)00227-9.

Diamond, L.W., 2003. Systematics of H_2O inclusions. In: Samson, I., Anderson, A., Marshall, D. (Eds.), Fluid Inclusions: Analysis and Interpretation. Mineralogical Association of Canada, Ottawa.

Dong, G., Morrison, G., Jaireth, S., 1995. Quartz textures in epithermal veins, Queensland; classification, origin and implication. Econ. Geol. 90, 1841–1856. https://doi.org/10.2113/gsecongeo.90.6.1841.

English, J.M., Laubach, S.E., 2017. Opening-mode fracture systems: insights from recent fluid inclusion microthermometry studies of crack-seal fracture cements. Geological Society, London, Special Publications 458, 257–272. https://doi.org/10.1144/sp458.1.

Fall, A., Bodnar, R.J., 2018. How precisely can the temperature of a fluid event be constrained using fluid inclusions? Econ. Geol. 113, 1817–1843. https://doi.org/10.5382/econgeo.2018.4614.

Fedor, F., Hámos, G., Jobbik, A., Máthé, Z., Somodi, G., Szűcs, I., 2008. Laboratory pressure pulse decay permeability measurement of Boda Claystone, Mecsek Mts., SW Hungary. Phys. Chem. Earth, Parts A/B/C 33, S45–S53. https://doi.org/10.1016/j.pce.2008.10.059.

Fitts, T.G., Brown, K.M., 1999. Stress-induced smectite dehydration: ramifications for patterns of freshening and fluid expulsion in the N. Barbados accretionary wedge. Earth Planet Sci. Lett. 172, 179–197. https://doi.org/10.1016/s0012-821x(99)00168-5.

Fodor, L., Csontos, L., Bada, G., Györfi, I., Benkovics, L., 1999. Tertiary tectonic evolution of the Pannonian Basin system and neighbouring orogens: a new synthesis of palaeostress data. Geological Society, London, Special Publications 156, 295–334. https://doi.org/10.1144/gsl.sp.1999.156.01.15.

Franks, P.C., 1969. Nature, origin, and significance of cone-in-cone structures in the Kiowa formation (early Cretaceous), North-central Kansas. SEPM J. Sediment. Res. 39, 1438–1454. https://doi.org/10.1306/74d71e51-2b21-11d7-8648000102c1865d.

Furukawa, Y., Barnes, H.L., 1995. Reactions forming pyrite from precipitated amorphous ferrous sulfide. In: Vairavamurthy, M.A., Schoonen, M.A.A., Eglinton, T.I., Luther, G. W., Manowitz, B. (Eds.), Geochemical Transformations of Sedimentary Sulfur. ACS Symposium Series, vol. 612, pp. 194–205. https://doi.org/10.1021/bk-1995-0612.ch010.

Gál, B., Poros, Zs, Ortega, E., 2020. Using fluid inclusion salinity data to reduce uncertainty in petrophysical Sw calculation – new application of an old technique in unconventional reservoirs. In: Paper Presented at the SPE/AAPG/SEG Unconventional Resources Technology Conference, Virtual. https://doi.org/10.15530/urtec-2020-2472. July 2020.

Goldstein, T.P., Aizenshtat, Z., 1994. Thermochemical sulfate reduction a review. J. Therm. Anal. 42, 241–290. https://doi.org/10.1007/bf02547004.

Goldstein, R.H., Reynolds, T.J. (Eds.), 1994. Systematics of Fluid Inclusions in Diagenetic Minerals. SEPM (Society for Sedimentary Geology). https://doi.org/10.2110/scn.94.31.

Haas, J., 2013. In: Hámor, G., Áron, J., Kovács, S., Nagymarosy, A., Szederkényi, T. (Eds.), Geology of Hungary. Springer Heidelberg, New York Dordrecht London. https://doi.org/10.1007/978-3-642-21910-8.

Hertelendi, E., 1996. A Bodai Aleurit Formációból Származó Mintákon Végzett Izotópanalitikai Vizsgálatok És Az Eredmények Értelmezése (Isotope Analysis and Interpretation on Samples from the Boda Clay Formation). Research Report. Isotoptech Bt., Debrecen (in Hungarian).

Hilgers, C., Urai, J.L., 2005. On the arrangement of solid inclusions in fibrous veins and the role of the crack-seal mechanism. J. Struct. Geol. 27, 481–494. https://doi.org/10.1016/j.jsg.2004.10.012.

Hilgers, C., Koehn, D., Bons, P.D., Urai, J.L., 2001. Development of crystal morphology during unitaxial growth in a progressively widening vein: II. Numerical simulations of the evolution of antitaxial fibrous veins. J. Struct. Geol. 23, 873–885. https://doi.org/10.1016/s0191-8141(00)00160-7.

Hoefs, J., 2009. Stable Isotope Geochemistry. Springer-Verlag Berlin Heidelberg. https://doi.org/10.1007/978-3-540-70708-0.

Horváth, F., Bada, G., Szafián, P., Tari, G., Ádám, A., Cloetingh, S., 2006. Formation and deformation of the Pannonian Basin: constraints from observational data. Geological Society, London, Memoirs 32, 191–206. https://doi.org/10.1144/gsl.mem.2006.032.01.11.

Horváth, F., Musitz, B., Balázs, A., Végh, A., Uhrin, A., Nádor, Á., Koroknai, B., Pap, N., Tóth, T., Wórum, G., 2015. Evolution of the Pannonian basin and its geothermal resources. Geothermics 53, 328–352. https://doi.org/10.1016/j.geothermics.2014.07.009.

Hrabovszki, E., Tóth, E., Raucsik, B., Varga, A., Schubert, F., 2017. Microstructure and cementation analyses on core samples from the BAF–2 well (Boda Claystone Formation, Mecsek mts). Bulletin of the Hungarian Geological Society 147, 245–264. https://doi.org/10.23928/foldt.kozl.2017.147.3.245 (in Hungarian with English abstract).

Hrabovszki, E., Tóth, E., Tóth, M.T., Máthé, Z., Schubert, F., 2020. Potential formation mechanisms of early diagenetic displacive veins in the Permian Boda Claystone Formation. J. Struct. Geol. 138, 104098. https://doi.org/10.1016/j.jsg.2020.104098.

Jébrak, M., 1997. Hydrothermal breccias in vein-type ore deposits: a review of mechanisms, morphology and size distribution. Ore Geol. Rev. 12, 111–134. https://doi.org/10.1016/s0169-1368(97)00009-7.

Kastner, M., Siever, R., 1979. Low temperature feldspars in sedimentary rocks. Am. J. Sci. 279, 435–479. https://doi.org/10.2475/ajs.279.4.435.

Kastner, M., Waldbaum, D.R., 1968. Authigenic albite from Rhodes. Am. Mineral. 53, 1579–1602.

Kastner, M., 1971. Authigenic feldspars in carbonate rocks. Am. Mineral. 56, 1403–1442.

Koehn, D., Passchier, C.W., 2000. Shear sense indicators in striped bedding-veins. J. Struct. Geol. 22, 1141–1151. https://doi.org/10.1016/s0191-8141(00)00028-6.

Konrád, Gy, Hámos, G., 2006. Geological aspects of determining high activity radioactive waste depository sites in Hungary and the results of the recent research. Acta geographica ac geologica et meteorologica Debrecina 1, 33–38 (in Hungarian with English abstract).

Konrád, Gy, Sebe, K., 2010. New details of young tectonic phenomena in the Western Mecsek Mts and their surroundings. Bulletin of the Hungarian Geological Society 140, 135–162 (in Hungarian with English abstract).

Konrád, Gy, Sebe, K., Halász, A., Babinszki, E., 2010. Sedimentology of a permian playa lake: the Boda Claystone Formation, Hungary. Geologos 16, 27–41. https://doi.org/10.2478/v10118-010-0002-1.

Lee, J.I., Lee, Y.I., 1998. Feldspar albitisation in Cretaceous non-marine mudrocks, Gyeongsang basin, Korea. Sedimentology 45, 745–754. https://doi.org/10.1046/j.1365-3091.1998.00173.x.

Lenti, F., Azbej, T., Németh, B., Szabó, Cs, 2010. Fluid inclusion study on the barite-calcite veins of the Boda Aleurolite formation (Mecsek mts., Hungary). Acta Minerol.-Petrogr. (Szeged). Abstract Series 06, 201.

Liutkus, C.M., Wright, J.D., 2007. The influence of hydrology and climate on the isotope geochemistry of playa carbonates: a study from Pilot Valley, NV, USA. Sedimentology 55, 965–978. https://doi.org/10.1111/j.1365-3091.2007.00932.x.

Lovering, T.G., 1972. Jasperoid in the United States – its characteristics, origin, and economic significance. USGS Professional Paper 710. https://doi.org/10.3133/pp710.

Luther, G.W., 1991. Pyrite synthesis via polysulfide compounds. Geochem. Cosmochim. Acta 55, 2839–2849. https://doi.org/10.1016/0016-7037(91)90449-f.

Machel, H.G., Krouse, H.R., Sassen, R., 1995. Products and distinguishing criteria of bacterial and thermochemical sulfate reduction. Appl. Geochem. 10, 373–389. https://doi.org/10.1016/0883-2927(95)00008-8.

Machel, H.G., 2001. Bacterial and thermochemical sulfate reduction in diagenetic settings – old and new insights. Sediment. Geol. 140, 143–175. https://doi.org/10.1016/s0037-0738(00)00176-7.

Maros, Gy, Koroknai, B., Palotás, K., Fodor, L., Dudko, A., Forián-Szabó, M., Zilahi-Sebess, L., Bán-Győri, E., 2004. Tectonic Analysis and Structural Evolution of the North-Eastern Mórágy Block. Annual report of the Geological Institute of Hungary, pp. 371–386, 2003.

Máthé, Z., Nádasi, J., 2017. A BAF–2 Fúrás Pirites Szakaszainak Vizsgálata (Investigation of Pyrite-Containing Sections in the BAF–2 Well). Research Report. Public Limited Company for Radioactive Waste Management (in Hungarian).

Máthé, Z., Varga, A., 2012. "Ízesítő" a permi Bodai Agyagkő Formáció őskörnyezeti rekonstrukciójához: kősó utáni pszeudomorfózák a BAT–4 fúrás agyagkőmintáiban ("Flavoring" for the environmental reconstruction of the Permian Boda Claystone Formation: Pseudomorphs after halite crystals in core samples from the BAT–4 well). Bulletin of the Hungarian Geological Society 142, 201–204 (in Hungarian).

Máthé, Z. (Ed.), 1999. A Bodai Aleurolit Formáció Minősítésének Rövidtávú Programja. Ásvány-Kőzettani, Kőzetgeokémiai És Izotóptranszport Vizsgálatok (Short-Term Program for the Certification of the Boda Siltstone Formation. Mineralogy, Rock Geochemistry and Isotope Transport Studies). Research Report. Mecsekérc Ltd., Pécs (in Hungarian).

Máthé, Z., 2015. Results of Mineralogical, Petrological and Geochemical Investigation of Boda Claystone Formation. PhD thesis. Eötvös Loránd University (in Hungarian with English summary).

Means, W.D., Li, T., 2001. A laboratory simulation of fibrous veins: some first observations. J. Struct. Geol. 23, 857–863. https://doi.org/10.1016/s0191-8141(00)00158-9.

O'Neil, J.R., Clayton, R.N., Mayeda, T.K., 1969. Oxygen isotope fractionation in divalent metal carbonates. J. Chem. Phys. 51, 5547–5558. https://doi.org/10.1063/1.1671982.

Pirajno, F., 2009. Hydrothermal Processes and Mineral Systems. Springer, Dordrecht. https://doi.org/10.1007/978-1-4020-8613-7.

Ramsay, J.G., Huber, M.I., 1983. The Techniques of Modern Structural Geology, vol. 1. Strain analysis. Academic Press, London.

Ramsay, J.G., 1980. The crack–seal mechanism of rock deformation. Nature 284, 135–139. https://doi.org/10.1038/284135a0.

Rickard, D., Luther, G.W., 1997. Kinetics of pyrite formation by the H_2S oxidation of iron (II) monosulfide in aqueous solutions between 25 and 125°C: the mechanism. Geochem. Cosmochim. Acta 61, 135–147. https://doi.org/10.1016/s0016-7037(96)00322-5.

Rickard, D., Luther, G.W., 2007. Chemistry of iron sulfides. Chem. Rev. 107, 514–562. https://doi.org/10.1021/cr0503658.

Rickard, D.T., 1975. Kinetics and mechanism of pyrite formation at low temperatures. Am. J. Sci. 275, 636–652. https://doi.org/10.2475/ajs.275.6.636.

Rickard, D., 1997. Kinetics of pyrite formation by the H_2S oxidation of iron (II) monosulfide in aqueous solutions between 25 and 125°C: the rate equation. Geochem. Cosmochim. Acta 61, 115–134. https://doi.org/10.1016/s0016-7037(96)00321-3.

Rosen, M.R., 1994. The importance of groundwater in playas: a review of playa classifications and the sedimentology and hydrology of playas. In: Rosen, M.R. (Ed.), Paleoclimate and Basin Evolution of Playa Systems. Geological Society of America. https://doi.org/10.1130/spe289-p1.

Saigal, G.C., Morad, S., Bjørlykke, K., Egeberg, P.K., Aagaard, P., 1988. Diagenetic albitization of detrital K-feldspar in Jurassic, Lower Cretaceous, and Tertiary clastic reservoir rocks from Offshore Norway, I. Textures and origin. SEPM J. Sediment. Res. 58, 1003–1013. https://doi.org/10.1306/212f8ee5-2b24-11d7-8648000102c1865d.

Sámson, M. (Ed.), 2015. BAF–2 Fúrás Dokumentáló És Értékelő Jelentése. (Documentation and Evaluation of the BAF–2 Well). Research Report. Public Limited Company for Radioactive Waste Management, Pécs (in Hungarian).

Sebe, K., 2017. Structural evolution of the Mecsek–Villány area (SW Hungary) during post-rift phase and basin inversion. In: Horvat, M., Wacha, L. (Eds.), 7th International Workshop "Neogene of Central and South-Eastern Europe". Velika, Croatia.

Sibson, R.H., Scott, J., 1998. Stress/fault controls on the containment and release of overpressured fluids: examples from gold-quartz vein systems in Juneau, Alaska; Victoria, Australia and Otago, New Zealand. Ore Geol. Rev. 13, 293–306. https://doi.org/10.1016/s0169-1368(97)00023-1.

Suchecki, R.K., Land, L.S., 1983. Isotopic geochemistry of burial-metamorphosed volcanogenic sediments, Great Valley sequence, northern California. Geochem. Cosmochim. Acta 47, 1487–1499. https://doi.org/10.1016/0016-7037(83)90308-3.

Taber, S., 1916. The growth of crystals under external pressure. Am. J. Sci. s4 (41), 532–556. https://doi.org/10.2475/ajs.s4-41.246.532.

Taylor, H.P., 1974. The application of oxygen and hydrogen isotope studies to problems of hydrothermal alteration and ore deposition. Econ. Geol. 69, 843–883. https://doi.org/10.2113/gsecongeo.69.6.843.

Török, K., 1994. Jelentés a Bodai Aleurolit Formációban Található Karbonátos Erek Folyadékzárványainak Vizsgálatáról (Report on the Investigation of Fluid Inclusions in Carbonate Veins from the Boda Siltstone Formation). Research Report. Eötvös Loránd University (in Hungarian).

Tóth, E., Hrabovszki, E., Tóth, M.T., Schubert, F., 2020. Shear strain and volume change associated with sigmoidal vein arrays in the Boda Claystone. J. Struct. Geol. 138, 104105. https://doi.org/10.1016/j.jsg.2020.104105.

Urai, J.L., Williams, P.F., van Roermund, H.L.M., 1991. Kinematics of crystal growth in syntectonic fibrous veins. J. Struct. Geol. 13, 823–836. https://doi.org/10.1016/0191-8141(91)90007-6.

Varga, A., Szakmány, Gy, Raucsik, B., Máthé, Z., 2005. Chemical composition, provenance and early diagenetic processes of playa lake deposits from the Boda Siltstone Formation (Upper Permian), SW Hungary. Acta Geol. Hung. 48, 49–68. https://doi.org/10.1556/ageol.48.2005.1.2.

Varga, A., Raucsik, B., Szakmány, Gy, Máthé, Z., 2006. Mineralogical, petrological and geochemical characteristics of the siliciclastic rock types of Boda Siltstone Formation. Bulletin of the Hungarian Geological Society 136, 201–231 (in Hungarian with English abstract).

Varga, A., 2009. Petrology and Geochemistry of the Paleozoic–Lower Triassic Siliciclastic Rocks from Southern Transdanubia, Hungary. PhD thesis. Eötvös Loránd University (in Hungarian with English summary).

Wilkin, R.T., Barnes, H.L., 1996. Pyrite formation by reactions of iron monosulfides with dissolved inorganic and organic sulfur species. Geochem. Cosmochim. Acta 60, 4167–4179. https://doi.org/10.1016/s0016-7037(97)81466-4.

Wiltschko, D.V., Morse, J.W., 2001. Crystallisation pressure versus "crack seal" as the mechanism for banded veins. Geology 29, 79–82. https://doi.org/10.1130/0091-7613(2001)029<0079:cpvcsa>2.0.co;2.

Woodland, B.G., 1964. The nature and origin of cone-in-cone structure. Fieldiana Geol. (New. Ser.) 13, 189–305. https://doi.org/10.5962/bhl.title.2709.